



# Spatial and cell type transcriptional landscape of human cerebellar development

Kimberly A. Aldinger<sup>1,2</sup>✉, Zachary Thomson<sup>1</sup>, Ian G. Phelps<sup>3</sup>, Parthiv Halripur<sup>1</sup>, Mei Deng<sup>3</sup>, Andrew E. Timms<sup>4</sup>, Matthew Hirano<sup>5</sup>, Gabriel Santpere<sup>6,7</sup>, Charles Roco<sup>8</sup>, Alexander B. Rosenberg<sup>5</sup>, Belen Lorente-Galdos<sup>6</sup>, Forrest O. Gulden<sup>6</sup>, Diana O'Day<sup>3</sup>, Lynne M. Overman<sup>9</sup>, Steven N. Lisgo<sup>9</sup>, Paula Alexandre<sup>10</sup>, Nenad Sestan<sup>6</sup>, Dan Doherty<sup>1,2,3</sup>, William B. Dobyns<sup>1,3,11</sup>, Georg Seelig<sup>5,12</sup>, Ian A. Glass<sup>1,2,3</sup> and Kathleen J. Millen<sup>1,3</sup>✉

The human neonatal cerebellum is one-fourth of its adult size yet contains the blueprint required to integrate environmental cues with developing motor, cognitive and emotional skills into adulthood. Although mature cerebellar neuroanatomy is well studied, understanding of its developmental origins is limited. In this study, we systematically mapped the molecular, cellular and spatial composition of human fetal cerebellum by combining laser capture microscopy and SPLiT-seq single-nucleus transcriptomics. We profiled functionally distinct regions and gene expression dynamics within cell types and across development. The resulting cell atlas demonstrates that the molecular organization of the cerebellar anlage recapitulates cytoarchitecturally distinct regions and developmentally transient cell types that are distinct from the mouse cerebellum. By mapping genes dominant for pediatric and adult neurological disorders onto our dataset, we identify relevant cell types underlying disease mechanisms. These data provide a resource for probing the cellular basis of human cerebellar development and disease.

The cerebellum, identified in classic neuroanatomy studies over 100 years ago, integrates neuronal networks that couple motor function with cognition, emotional regulation and language<sup>1,2</sup>. Its unique structure and function depend on the precise developmental coordination of molecular and cellular programs among multiple cell types<sup>3,4</sup> and, when these go awry, result in disease. Cerebellar diseases include congenital structural abnormalities in children and cerebellar ataxias in adults that have specific cerebellar pathology but also disorders that affect multiple brain regions, including the cerebellum, such as autism spectrum disorders (ASDs) and Alzheimer's disease (AD)<sup>1,5–7</sup>. Although cerebellar development is relatively well understood in mice<sup>8,9</sup>, we have only begun to unravel the complexity and dynamics of human cerebellar development.

Cerebellar spatial organization results from timed cellular proliferation and differentiation within distinct progenitor niches and coordinated cell migration during development<sup>10–12</sup>. A unique feature of the human cerebellum is that the progenitor zones have extended proliferative activity, suggesting human-specific expansion of these zones<sup>10</sup>. Emerging from the dorsal hindbrain, the cerebellar anlage contains two separate proliferative niches: the ventricular zone (VZ), which lines the fourth ventricle, and the rhombic lip (RL), which is dorsal to the VZ and adjacent to the developing choroid plexus. The VZ, which gives rise to GABAergic neurons, is active during early embryonic stages and dominates the cerebellar anlage

with nascent VZ-derived Purkinje cells by 10 post-conceptional weeks (PCW) (Fig. 1a). After 10 PCW, the RL expands to generate glutamatergic neurons, most of which are granule cell progenitors (GPCs), which migrate rostrally to form the external granule cell layer (EGL) on the dorsal surface. By mid-gestation, Purkinje cells reorganize into a single-cell layer (known as the Purkinje cell layer (PCL)) under the EGL. At the same time, GPCs in the EGL proliferate, differentiate and migrate inward to form the internal granule cell layer located just below the PCL.

Many core molecular programs and cellular cues that guide the extensive growth and coordinated reorganization during cerebellar development are known<sup>3,8,9</sup>. However, cerebellum is not well represented in previous bulk and single-cell transcriptomic studies of the developing human brain<sup>13–17</sup>. In the BrainSpan atlas of the developing human brain, samples from neocortical regions account for 68% (415/607) of the samples<sup>15</sup>. In contrast, cerebellar samples account for only 6% (35/607) of the total samples (Supplementary Fig. 1). Prenatal development of the cerebellum is even less well represented in BrainSpan, with cerebellum comprising only 5% (13/261) of the prenatal samples (8–37 PCW). Furthermore, the available data are predominantly derived from bulk transcriptomic analysis. As it stands, the available human brain transcriptomic data are not likely to capture the depth and breadth of the molecular repertoire in the cerebellum, especially during early development.

<sup>1</sup>Center for Integrative Brain Research, Seattle Children's Research Institute, Seattle, WA, USA. <sup>2</sup>Brotman Baty Institute for Precision Medicine, Seattle, WA, USA. <sup>3</sup>Department of Pediatrics, University of Washington, Seattle, WA, USA. <sup>4</sup>Center for Developmental Biology and Regenerative Medicine, Seattle Children's Research Institute, Seattle, WA, USA. <sup>5</sup>Department of Electrical and Computer Engineering, University of Washington, Seattle, WA, USA.

<sup>6</sup>Department of Neuroscience and Kavli Institute for Neuroscience, Yale School of Medicine, New Haven, CT, USA. <sup>7</sup>Neurogenomics Group, Research Programme on Biomedical Informatics, Hospital del Mar Medical Research Institute, Department of Experimental and Health Sciences, Universitat Pompeu Fabra, Barcelona, Spain. <sup>8</sup>Department of Bioengineering, University of Washington, Seattle, WA, USA. <sup>9</sup>Biosciences Institute, Faculty of Medical Sciences, Newcastle University, Newcastle upon Tyne, UK. <sup>10</sup>University College London Great Ormond Street Institute of Child Health, London, UK.

<sup>11</sup>Department of Neurology, University of Washington, Seattle, WA, USA. <sup>12</sup>School of Computer Science and Engineering, University of Washington, Seattle, WA, USA. ✉e-mail: [kimberly.aldinger@seattlechildrens.org](mailto:kimberly.aldinger@seattlechildrens.org); [kathleen.millen@seattlechildrens.org](mailto:kathleen.millen@seattlechildrens.org)

Here we characterize the transcriptional and cellular landscape of the developing human cerebellum by combining laser capture microdissection (LCM) of spatially defined progenitor and neuronal populations with single-nucleus transcriptomic sequencing. We report single-nucleus combinatorial indexing that profiles the transcriptomes of 70,000 cells across prenatal cerebellar development from 9 to 21 PCW. We cross-compare these data with the BrainSpan dataset and with a published mouse dataset. Our work establishes a ‘Developmental Cell Atlas of the Human Cerebellum’ as a solid foundation, enabling novel discoveries related to cerebellar development and origin of disease.

## Results

**Study design and data generation.** To characterize the transcriptional landscape of the prenatal human cerebellum, we generated and analyzed transcriptomic data using direct and inferred approaches to define cell populations. We performed bulk RNA sequencing (RNA-seq) from spatially demarcated progenitor and neuronal regions isolated by LCM (57 samples from 16 cerebella) and single-cell RNA-seq (69,174 cells/nuclei from 13 cerebella) from 29 postmortem cerebella obtained from clinically and histopathologically unremarkable donors of both sexes across fetal development (Fig. 1b and Supplementary Tables 1 and 2).

To obtain populations preferentially enriched for primary progenitors and neurons, we devised a consistent experimental workflow to isolate cells occupying RL, EGL and PCL (Fig. 1b and Extended Data Fig. 1a). Specifically, we dissected whole cerebella from fetal specimens with intact calvaria (the top part of the skull) to ensure correct orientation for each sample and sectioned frozen cerebella in the sagittal plane through the cerebellar midline lobe (vermis). We then isolated RNA from one section for each specimen (referred to hereafter as ‘bulk’) and assessed RNA quality (RNA integrity number,  $7.7 \pm 0.95$  (mean  $\pm$  s.d.)) (Supplementary Table 1). For our LCM sample collection, we visually localized the EGL, which is easily identifiable in sagittal sections as a cell-dense layer on the dorsal surface of the developing cerebellar anlage, and attained adjacent sections using an anti-calbindin antibody, a well-known Purkinje cell marker, to identify the PCL. Finally, we isolated total RNA from our 57 samples. We previously performed LCM and RNA-seq of the RL<sup>10</sup> and included this dataset in our analysis.

For our sequencing libraries, we selected the Illumina TruSeq RNA Access Library Prep Kit because it requires low total RNA input yet maintains high sensitivity. We then performed paired-end Illumina high-quality sequencing on bulk cerebellum ( $n=13$ ), RL ( $n=9$ ), EGL ( $n=17$ ) and PCL ( $n=18$ ) from 16 mid-gestation (9–21 PCW) fetal specimens (Fig. 1b and Supplementary Table 1). By comparing gene expression of established RL (*LMX1A* and *BARHL1*), EGL (*ATOH1* and *PAX6*) and PCL (*CALB1* and *SKOR2*) markers between the RNA-seq dataset from LCM-isolated samples and bulk-isolated cerebellum, we validated the technical quality of our LCM isolation; expression of these six neuron-specific markers confirmed the specificity of our enrichment, with the highest expression detected in the appropriate samples (Extended Data Fig. 1b).

To complement our spatially defined analyses, we performed three single-nucleus RNA sequencing (snRNA-seq) experiments using 26 samples from an independent set of 13 cerebella ranging in age from 9 to 21 PCW (Fig. 1c and Supplementary Table 2). We used split-pool ligation-based transcriptome sequencing (SPLiT-seq), a multistep barcoding strategy combined with RNA-seq that increases throughput by enabling simultaneous interrogation of thousands of cells/nuclei in multiplexed samples<sup>18</sup>. Single-cell-level (eight samples) and single-nucleus-level (12 samples) transcriptomic data were generated in technical replicates for ten cerebella across two experiments; data for the remaining three cerebella were generated in a single experiment.

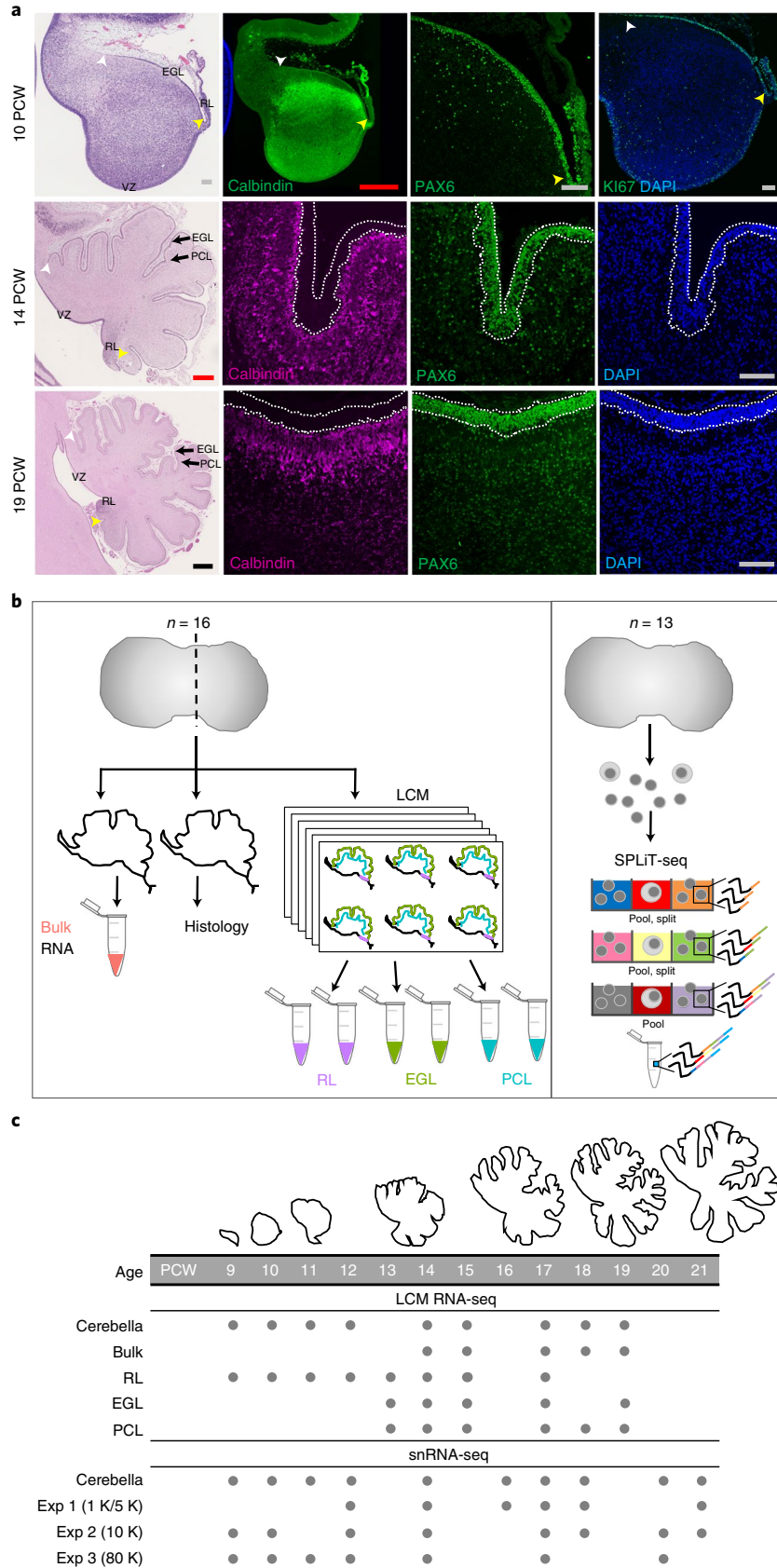
**Transcriptional analysis of spatially defined neural zones.** To characterize the global transcriptional landscapes in RL, EGL and PCL, we applied principal component analysis (PCA) to the expression profiles of LCM-isolated regionally distinct regions and from bulk cerebellum. PCA visualized sample clustering corresponding to neuronal region, with PC1 distinguishing RL and EGL from PCL and bulk cerebellum and PC2 distinguishing RL from EGL (Fig. 2a). To identify spatially regulated genes, we evaluated differential gene expression between each LCM-isolated zone and bulk cerebellum using a modest threshold (false discovery rate (FDR)  $< 0.05$  and log<sub>2</sub>-transformed fold change (FC)  $> 1.5$ ) and including library prep batch, age and region as covariates (Fig. 2b–d). This analysis identified 1,111 differentially expressed genes (1.5-fold, FDR  $< 0.05$ ) among the neuronal zones: 627 genes showed increased expression in RL, 612 genes showed increased expression in EGL and 168 genes showed increased expression in PCL compared to bulk cerebellum (Fig. 2e and Supplementary Table 3). The RL genes were enriched for cell cycle (*hsa04110*, FDR =  $1.2 \times 10^{-18}$ ) and p53 signaling pathways (*hsa04115*, FDR =  $6.3 \times 10^{-6}$ ), as were the EGL genes (*hsa04110*, FDR =  $1.1 \times 10^{-14}$  and *hsa04115*, FDR = 0.0007) (Supplementary Table 4). The PCL genes showed little pathway enrichment. Subsets of genes were specifically expressed in each captured region (Supplementary Fig. 2): 184 RL-specific genes, 176 EGL-specific genes and 142 PCL-specific genes. The RL genes were enriched in Hippo signaling, stem cell pluripotency regulation and TGF-β signaling (Fig. 2f), with expression increasing across mid-gestation (Supplementary Fig. 2d). EGL genes were enriched in MAPK, Ras and Rap1 signaling (Fig. 2g and Supplementary Fig. 2e). Again, we detected little pathway enrichment among PCL genes (Supplementary Table 4).

To identify cellular components of the spatial cerebellar transcriptome, we performed weighted gene co-expression network analysis (WGCNA)<sup>19</sup> on all 57 LCM samples and identified 21 modules of co-expressed genes (Extended Data Figs. 2–4 and Supplementary Tables 5 and 6). We curated 21 gene co-expression modules according to spatial relationships among enriched regions and shared gene expression among regions within the RL lineage. Of these, nine modules showed expression differences among cerebellar regions (spatial); eight modules showed expression

**Fig. 1 | Overview of prenatal cerebellar development and the data generated in this study.** **a**, Midsagittal sections of the human fetal cerebellum stained with hematoxylin and eosin (H&E) or markers for Purkinje cells (calbindin) or RL and EGL (*PAX6* and *KI67*). A minimum of two samples per age were stained with adjacent sections used for histology and immunocytochemistry. The VZ, RL, EGL and PCL are shown. Arrowheads mark the anterior (yellow) and posterior (white) EGL across the dorsal surface of the cerebellar anlage. At 9 PCW, the cerebellar anlage is dominated by Purkinje cells, with a thin nascent EGL extending from the RL. By 19 PCW, Purkinje cells have migrated radially to establish a multicellular layer (PCL) beneath the EGL. Scale bars, 100 µm (gray), 500 µm (red) and 1 mm (blue). An H&E-stained section at 10 PCW was used previously in Fig. 1 of Haldipur et al.<sup>10</sup>. **b**, Schematic illustrating LCM (left) and SPLiT-seq (right) experimental workflows. **c**, The time span of fetal cerebellar development represented by line drawings of midsagittal sections of the cerebellum (to scale) showing a dramatic change in size and foliation from 9 to 19 PCW. Below is the distribution of cerebella in this study. Biological and technical replicate samples are not shown (RNA-seq sample numbers:  $n=13$  for bulk,  $n=9$  for RL,  $n=17$  for EGL and  $n=18$  for PCL; snRNA-seq sample numbers:  $n=6$  for Exp 1,  $n=11$  for Exp 2 and  $n=9$  for Exp 3).

differences in both RL and EGL (RL lineage); one module was enriched in bulk cerebellum; and three modules did not show differential expression among the regions captured.

When we compared our 21-gene co-expression modules to the 73 modules generated in the most recent BrainSpan analysis of human neurodevelopment<sup>15</sup>, which comprises 16 anatomical brain



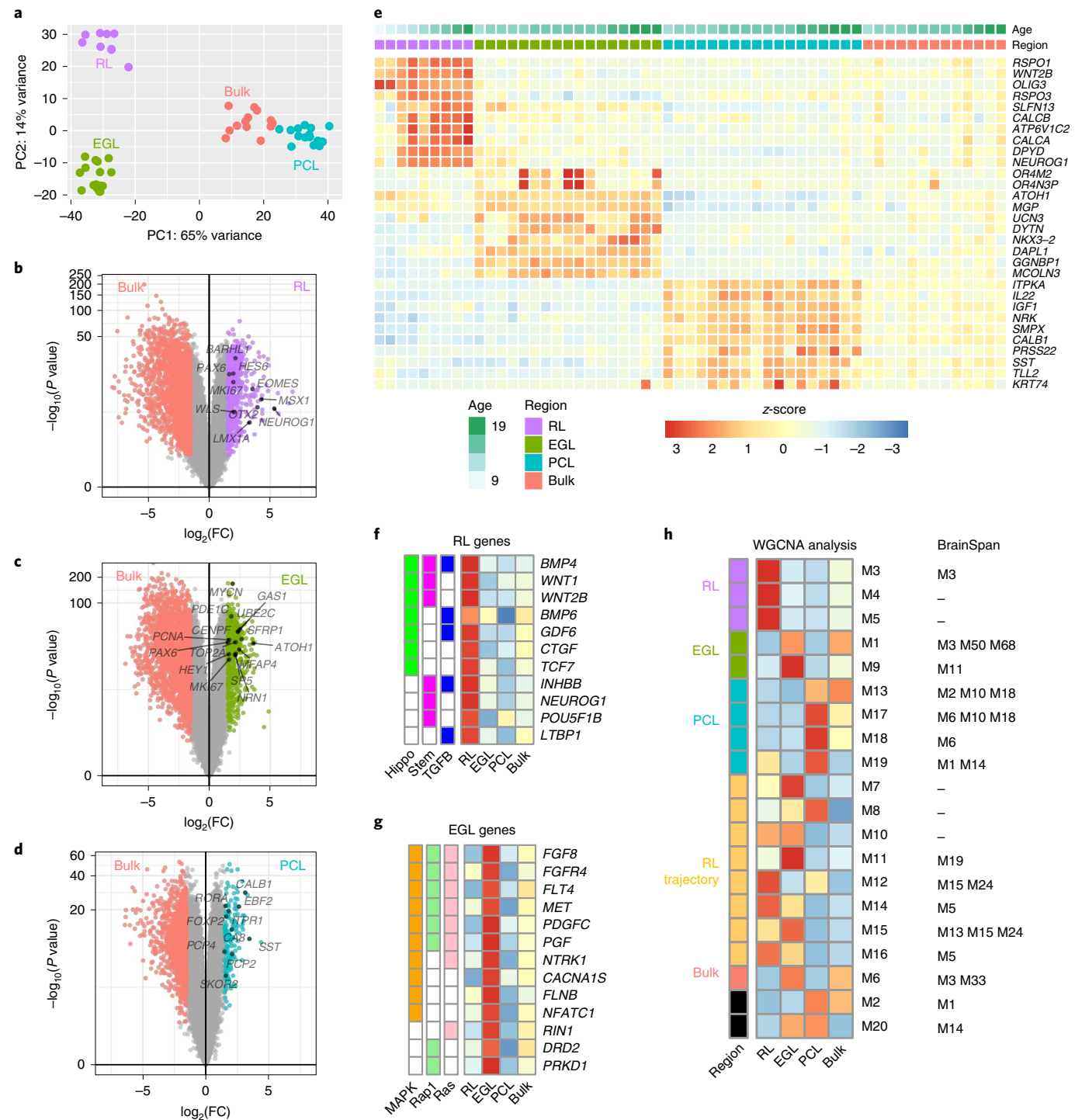


**Fig. 2 | Spatial transcriptional analysis of the developing human cerebellum.** **a**, PCA indicates that the largest source of variation among RNA-seq samples was spatial location, accounting for 57% of the variance, and verifies that LCM successfully captured these regions. **b-d**, Volcano plots illustrating differential expression of genes for each spatial region versus bulk cerebellum. Colored dots represent genes with significant expression ( $FDR < 0.05$ ,  $\log_2(\text{FC}) > 1.5$ ). Selected canonical genes with significant expression are labeled. Significance was determined by the Wald test and adjusted using FDR. Statistics are presented in Supplementary Table 3. **e**, Heat map of the top ten genes with significant expression per spatial region (RL, EGL and PCL) are shown for each sample. Samples are ordered by region (RL (purple), EGL (green), PCL (turquoise) and bulk (salmon)) and then by ascending age (9–19 PCW). High expression is in red, and low expression is in blue. **f,g**, Heat maps of genes and pathways expressed in RL (**f**) and EGL (**g**) identified by Gene Ontology analysis. High expression is in red, and low expression is in blue; z-score legend as in **e**. Colored boxes indicate genes represented in enriched pathways: Hippo signalling (green), signalling pathways regulating pluripotency of stem cells (magenta) and TGF- $\beta$  signalling (blue) in **f**; MAPK signalling (orange), Rap1 (green) and Ras (pink) in **g**. Statistics are presented in Supplementary Table 4. **h**, Heat map of genes expressed in each WGCNA module enriched in **a**. High expression is in red, and low expression is in blue; z-score legend as in **e**. Colored boxes represent the cerebellar region interpretation for each WGCNA module, as in Supplementary Table 5.

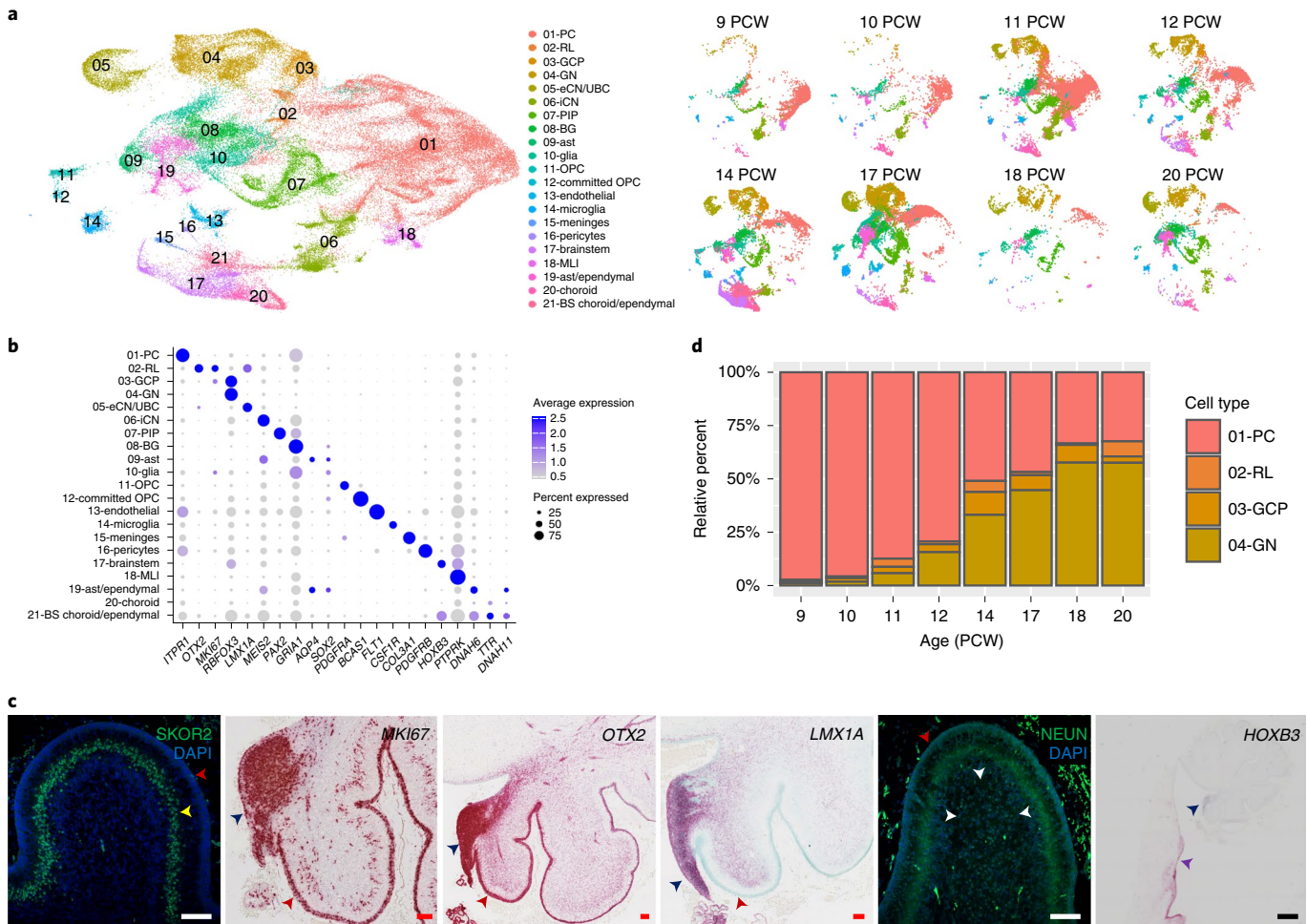


**Fig. 3 | Identifying the major cell types of the developing human cerebellum.** **a**, UMAP visualization of 67,174 human cerebellar nuclei colored by cluster identity from Louvain clustering and annotated on the basis of marker genes. The same UMAP is plotted at right, showing only nuclei from each age (nuclei numbers from left to right:  $n=5,003$  for 9 PCW;  $n=2,329$  for 10 PCW;  $n=20,364$  for 11 PCW;  $n=7,119$  for 12 PCW;  $n=11,213$  for 14 PCW;  $n=15,556$  for 17 PCW;  $n=1,617$  for 18 PCW; and  $n=5,177$  for 20 PCW). **b**, Dot plot showing the expression of one selected marker gene per cell type. The size of the dot represents the percentage of nuclei within a cell type in which that marker was detected, and its color represents the average expression level. Statistics are presented in Supplementary Table 9. **c**, Midsagittal sections of the human fetal cerebellum at 18 PCW stained with selected marker genes for Purkinje cells (SKOR2), proliferation (MKL67), RL (OTX2 and LMX1A), GNs (NEUN) and brainstem (HOXB3). Adjacent sections from one sample were stained for OTX2 and HOXB3; a minimum of three sections from each of three samples were stained for the other markers. The EGL, PCL, internal granule cell layer, RL and brainstem are indicated by red, yellow, white, blue and purple arrowheads, respectively. Sections are counterstained using DAPI for immunohistochemistry (SKOR2 and NEUN) or Fast Green for *in situ* hybridization (MKL67, OTX2, LMX1A and HOXB3). Scale bar, 100  $\mu$ m and 1 mm (HOXB3). LMX1A was used previously in Fig. 3g of Haldipur et al.<sup>10</sup> **d**, Stacked bar charts show the percentage of the four major cell types from each age sampled. Bar colors represent Purkinje cells (PCs), rhombic lip (RL), granule cell progenitors (GCPs) and granule neurons (GNs).

regions including cerebellar cortex, we found that 26 of the 73 BrainSpan modules were correlated with the modules derived from our data (Fig. 2h and Supplementary Fig. 3). We found that genes in 14 BrainSpan modules were enriched among genes with spatial expression in prenatal cerebellum, eight of which were enriched in the RL lineage (RL and EGL), two of which were enriched in the bulk cerebellum and two of which were correlated with modules that were not differentially expressed in the prenatal cerebellum. Overall, most of these 14 BrainSpan modules were highly expressed prenatally in all brain regions and contained multiple neural and non-neural cell types (Supplementary Table 3). Among the 15 cerebellar-specific BrainSpan modules, only one (M11) was shared with our data (M9). The M11 module is highly expressed in postnatal cerebellum and includes granule cell markers, such as *PAX6* and *GABRA6*. This result was expected given that our data are exclusively prenatal, when Purkinje cells dominate, whereas BrainSpan

contains a small number of primarily postnatal cerebellum samples, when the granule cell population is vastly dominant relative to all other cell types in the cerebellum<sup>20</sup>. In our data, *PAX6* is found in M14, which is highly expressed in both RL and EGL, consistent with the granule neuron (GN) lineage, and enriched in processes regulating DNA (Supplementary Table 6).

**Cell types in the developing human cerebellum.** We performed snRNA-seq to define cell types and assemble cell-type-specific transcriptomes in the developing human cerebellum from 9 to 21 PCW (Supplementary Table 2). Using SPLiT-seq<sup>18</sup>, we sequenced 92,314 nuclei (~21,000 raw reads per nucleus) with a median transcript capture of 1,214 unique molecular identifiers (UMIs) per nucleus (Supplementary Table 7). We removed outlier cells with too few (<200) or too many (dataset-specific cutoffs) genes detected. We used DoubletFinder<sup>21</sup> to detect and discard 5% likely doublets.

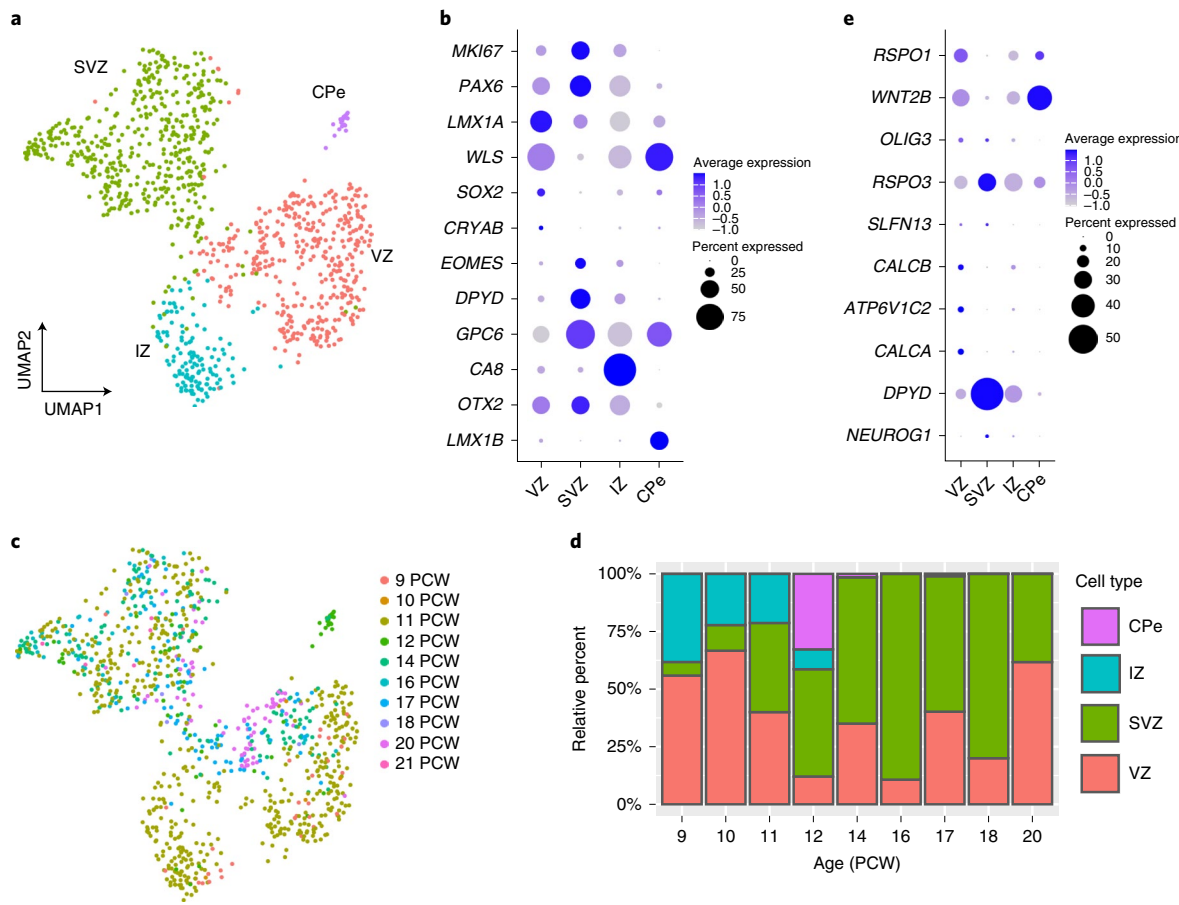


**Fig. 4 | Analysis of RL compartments at single-cell resolution.** **a**, UMAP visualization and marker-based annotation of the RL subclusters ( $n=1,018$  nuclei;  $n=466$  for SVZ;  $n=390$  for VZ;  $n=135$  for IZ; and  $n=21$  for CPe). CPe, choroid plexus epithelium; IZ, intermediate zone; SVZ, subventricular zone; VZ, ventricular zone. **b**, Dot plot showing the expression of selected marker genes in subclusters. **c**, The same UMAP as in **a** with nuclei colored by sample age ( $n=34$  for 9 PCW;  $n=9$  for 10 PCW;  $n=535$  for 11 PCW;  $n=58$  for 12 PCW;  $n=137$  for 14 PCW;  $n=56$  for 16 PCW;  $n=97$  for 17 PCW;  $n=5$  for 18 PCW;  $n=81$  for 20 PCW; and  $n=6$  for 21 PCW). **d**, Stacked bar charts show the percentage of the RL subclusters by sample age. **e**, Dot plot showing the expression of the top ten most differentially expressed genes from the spatial transcriptional analysis of the RL (Fig. 2e and Supplementary Table 3).

The remaining 69,174 nuclei had an average of 3,626 transcripts/UMIs per nucleus from 1,332 genes. We merged a total of four datasets: two datasets generated previously<sup>22</sup> and two datasets generated in the present study. Each dataset was filtered independently, after which we used Seurat version 3 (ref.<sup>23</sup>) to integrate all four datasets. We applied Louvain clustering and uniform manifold approximation and projection (UMAP) visualization to all cells in the integrated dataset (Fig. 3a). Nuclei from replicate samples processed in separate experiments were similarly distributed, whereas nuclei from different developmental stages were not (Extended Data Fig. 5). We used known marker genes to manually annotate 21 distinct cell types and then validated the expression of selected marker genes using immunohistochemistry or *in situ* hybridization (Fig. 3b,c and Supplementary Table 8).

Across the 21 major cell types, 4,443 genes ( $FDR < 0.05$ ) were differentially expressed (Supplementary Table 9). We identified 239 cell-type-specific marker genes (average  $\log FC > 1.5$ ; Extended Data Fig. 6), many that were previously characterized as markers of the respective cell types. For example, we detected *CA8*, *ITPR1*, *DAB1* and *RORA* in Purkinje cells, *SLIT2* in RL and *RELN* and *RBFOX3* in GNs.

The 21 cell types as a group are represented by a median of 1,659 nuclei (ranging from 25,724 Purkinje cells to 189 pericytes). Across developmental time points, our analysis mirrored known changes in the cellular composition of the four major cerebellar cell

types (Purkinje cells, RL, GPCs and GNs) (Fig. 3d). For instance, at 9 PCW, Purkinje cells comprised 97% (3,736/3,839) of the total nuclei recovered from the major cell types present and then gradually declined to 32% (371/1,145) at 20 PCW. Conversely, GNs in the cerebellar anlage at 9 PCW comprised 1% (44/3,839) of the total nuclei recovered and then increased across development to reach 58% (659/1,145) at 20 PCW. Cell type composition among samples was most consistent in our largest dataset (Extended Data Fig. 7). Overall, RL comprised only 1% (1,018/69,174) of the total nuclei recovered from the cerebellum across development, with 822 (81%) RL nuclei detected among 59,608 total nuclei recovered in our largest dataset (Extended Data Fig. 5a and Supplementary Table 7).

**Molecular distinction between RL compartments.** We recently demonstrated that the human RL has unique cytoarchitectural features that are not shared with other vertebrates, including the non-human primate macaque<sup>10</sup>. Specifically, in human fetal brain development, the RL begins as a simple proliferative progenitor niche but then becomes compartmentalized into ventricular zones (RL<sup>VZ</sup>) and subventricular zones (RL<sup>SVZ</sup>), which persist until birth. To identify molecular characteristics of the uniquely human RL progenitor subsets, we selected and subclustered cells in the RL population and examined the molecular correlates that define the RL<sup>VZ</sup> and RL<sup>SVZ</sup> compartments (Fig. 4). To annotate

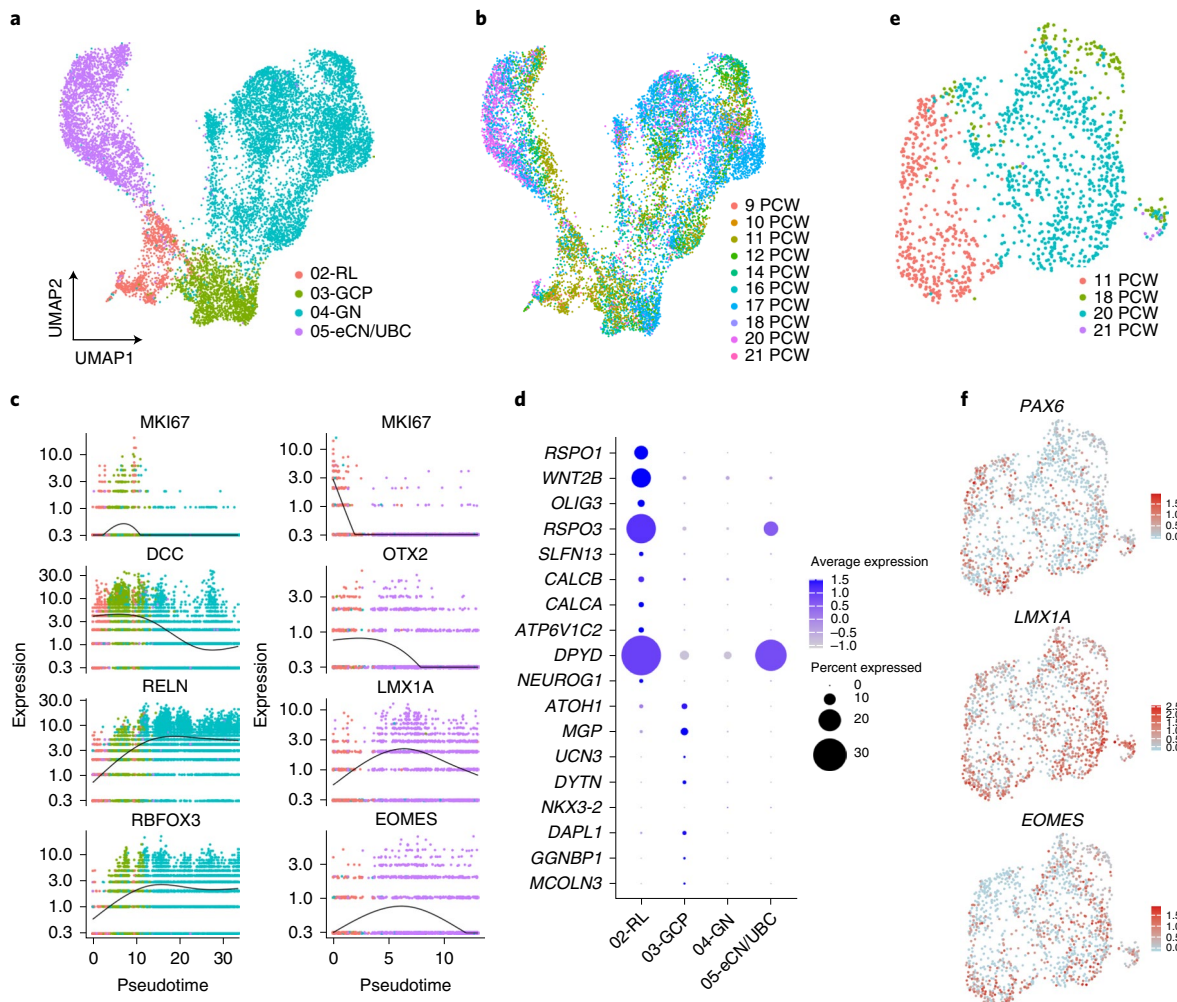


**Fig. 5 | Characterization of the RL trajectory.** **a**, UMAP visualization and marker-based annotation of cell types that originate from the RL ( $n=12,243$ :  $n=1,018$  for RL;  $n=1,659$  for GCP;  $n=6,727$  for GN; and  $n=2,839$  for eCN/UBC). **b**, The same UMAP as in **a** with nuclei colored by sample age ( $n=120$  for 9 PCW;  $n=61$  for 10 PCW;  $n=2,190$  for 11 PCW;  $n=1,053$  for 12 PCW;  $n=1,663$  for 14 PCW;  $n=432$  for 16 PCW;  $n=4,410$  for 17 PCW;  $n=627$  for 18 PCW;  $n=1,626$  for 20 PCW; and  $n=89$  for 21 PCW). **c**, Kinetics plot showing the relative expression of RL trajectory marker genes across developmental pseudotime. Dots are colored according to cell types as in **a**. **d**, Dot plot showing the expression of the top ten most differentially expressed genes from the spatial transcriptional analysis of RL and EGL (Fig. 2e and Supplementary Table 3). **e**, UMAP visualization of the eCN/UBC cluster including 11-, 18-, 20- and 21-PCW samples. Nuclei are colored by sample age ( $n=1,424$ ;  $n=436$  for 11 PCW;  $n=138$  for 18 PCW;  $n=842$  for 20 PCW; and  $n=8$  for 21 PCW). **f**, The same UMAP as in **e** with nuclei colored by expression level for the indicated gene.

the subclusters, we first examined the expression of classic RL markers. Indeed, *MKI67*, *PAX6* and *LMX1A* were expressed throughout the subclusters, consistent with their known expression as RL markers. *WLS*, *SOX2* and *CRYAB* were restricted to one subcluster, identifying it as the  $\text{RL}^{\text{VZ}}$  (Fig. 4b and Supplementary Table 10). Another subcluster expressed *CA8*, suggesting that they are likely Purkinje cells originating from the intermediate zone, and another expressed *LMX1B*, consistent with choroid plexus epithelium. We observed marked changes in the proportions of cells within RL compartments during development, with the proportion of cells occupying the  $\text{RL}^{\text{VZ}}$  generally decreasing across development and cells in the  $\text{RL}^{\text{SVZ}}$  increasing. Next, we identified additional genes with RL spatially restricted expression. We selected the top RL markers defined by our spatial RNA-seq analysis (Fig. 2f) and examined expression at the single-cell level within the RL subclusters (Fig. 4e). *OLIG3*, *RSPO3* and *SLFN13* were expressed throughout the RL, whereas *WNT2B*, *CALCB*, *ATP6V1C2* and *CALCA* were expressed in the  $\text{RL}^{\text{VZ}}$ , and *DPYD* expression was enriched in the  $\text{RL}^{\text{SVZ}}$ .

**Developmental trajectory of the RL lineage.** The RL gives rise to all glutamatergic neuronal subtypes of the developing cerebellum in a sequential manner<sup>24,25</sup>. First, glutamatergic neurons destined to become excitatory cerebellar interneurons (eCNs), which integrate GABAergic Purkinje cell-mediated and excitatory mossy fiber/climbing inputs to serve as major output tracts, are generated. Second, GCPs that proliferate, differentiate and migrate to form the internal granule layer arise. Lastly, unipolar brush cell (UBC) interneurons that make pre-synaptic connections with vestibular ganglia and nuclei are formed<sup>24,26</sup>. To resolve lineage trajectories of the RL, GCP, GN and eCN/UBC subpopulations, we subclustered the cells and ordered them according to pseudotime using Monocle 3 (ref. 27) (Fig. 5a,b). We confirmed predicted developmental trajectories, including temporal progression and expression of classic markers, with one branch of the RL trajectory giving rise to GCPs and then GNs, and the second branch giving rise to eCNs/UBCs (Fig. 5b). As progenitors differentiate into eCNs/UBCs, canonical RL gene expression (*MKI67*, *OTX2*, *LMX1A* and *EOMES*) declines, and as GCPs differentiate into GNs, *MKI67*

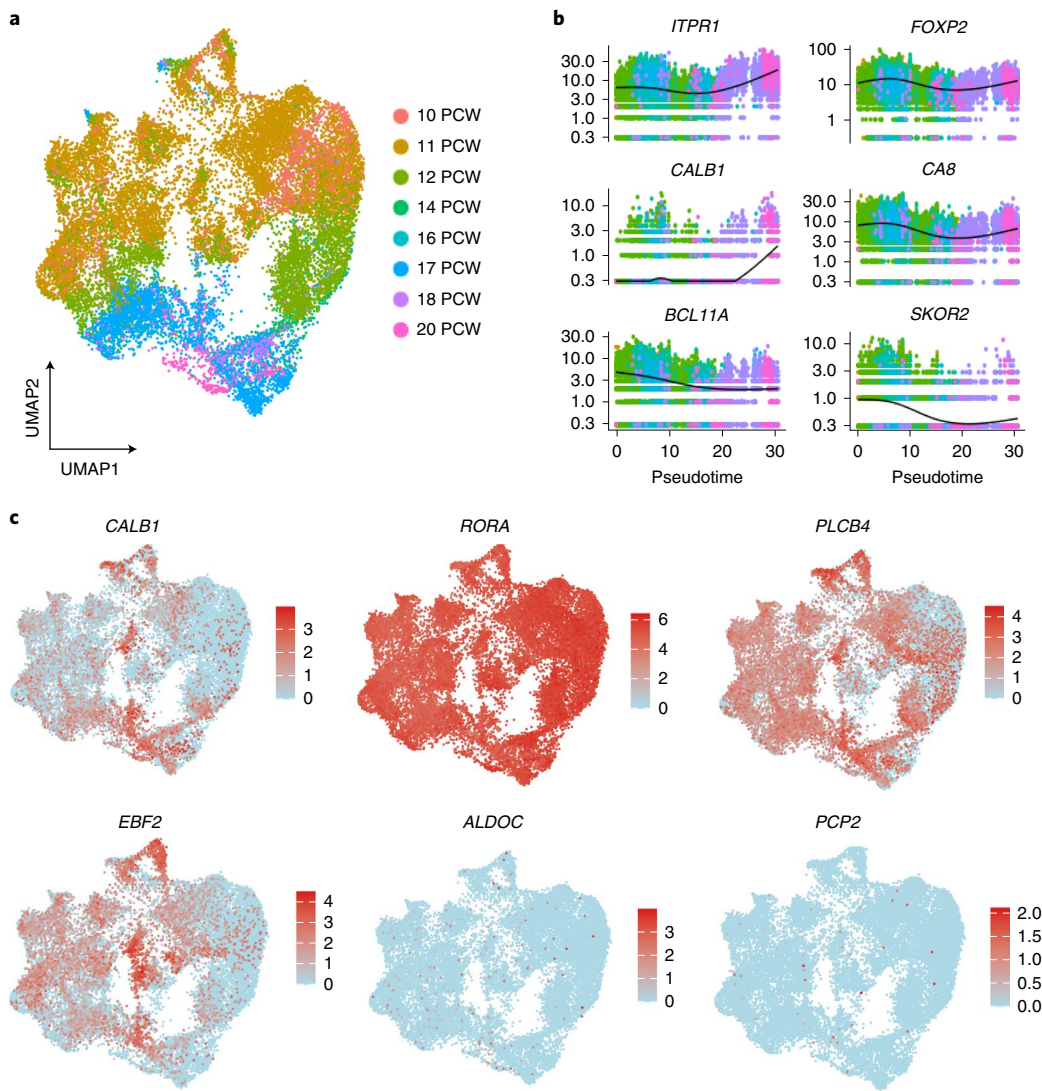


**Fig. 6 | Purkinje cells.** **a**, UMAP visualization of the PC cluster. Nuclei are colored by sample age ( $n=25,724$ ;  $n=3,736$  for 9 PCW;  $n=1,131$  for 10 PCW;  $n=12,182$  for 11 PCW;  $n=3,543$  for 12 PCW;  $n=1,346$  for 14 PCW;  $n=26$  for 16 PCW;  $n=3,144$  for 17 PCW;  $n=245$  for 18 PCW; and  $n=371$  for 20 PCW). **b**, Kinetics plot showing the relative expression of PC marker genes across developmental pseudotime. Dots are colored by sample age as in **a**. **c**, The same UMAP as in **a** with nuclei colored by expression level for the indicated gene.

and *DCC* expression in GCPs declines concurrent with increased expression of *RELN* and *RBOX3*. As we had done for the RL compartments, we selected the top markers for RL and EGL defined by our spatial RNA-seq analysis (Fig. 2e) and examined expression of these marker genes at the single-cell level within the RL trajectory (Fig. 5c). Among the top ten RL markers, *RSPO1*, *WNT2B*, *OLIG3*, *SLFN13*, *CALCB*, *CALCA* and *ATP6V1C2* expression was largely confined to the RL lineage, whereas *RSPO3* and *DYPD* expression was highest in both RL and eCNs/UBCs. Among the top ten EGL markers, expression was largely confined to the GCPs, although the overall magnitude of expression was low.

Consistent with their RL origin, eCNs and UBCs express the classic RL markers *PAX6*, *LMX1A* and *EOMES*<sup>26,28</sup>. We identified eCNs/UBCs on the basis of these markers and the absence of *MKI67* expression (because eCNs and UBCs are non-proliferative at the ages sampled) (Fig. 3a,b and Supplementary Tables 8 and 9). The cells within this cluster were present in all ages sampled (9–21 PCW) and were distinct from other glutamatergic neurons (GCPs and GNs) that also originate from RL neural progenitors (Fig. 5). To more clearly delineate the different developmental origins of

eCNs and UBCs, we selected cells in the eCN/UBC population from 11 PCW or 18–21 PCW, subclustered the cells and examined the molecular correlates that define eCN and UBC (Fig. 5). We found that *PAX6*, *LMX1A* and *EOMES* were expressed throughout this cluster. Although we attempted to distinguish eCNs and UBCs by examining *LMX1A/EOMES* co-expression in the eDCN/UBC cluster, only a few co-expressing cells were detectable (Extended Data Fig. 8), limiting this analysis.

**Purkinje cells dominate the developing cerebellar anlage.** In the adult brain, Purkinje neurons form a single layer with extensive dendritic arborization in the molecular layer and axons projecting to the deep cerebellar nuclei to coordinate all motor output. By 10 PCW, inhibitory Purkinje neurons dominate the cerebellar anlage<sup>29</sup> and, as expected, represented the cell type with the most nuclei recovered in our dataset (Fig. 3). Nuclei within this cluster were present in all ages sampled (9–21 PCW) and were distinct from other GABAergic neurons (inhibitory cerebellar nuclei and *PAX2*<sup>+</sup> interneuron progenitors (PIPs)) that also originate from VZ neural progenitors. To examine early markers of human Purkinje

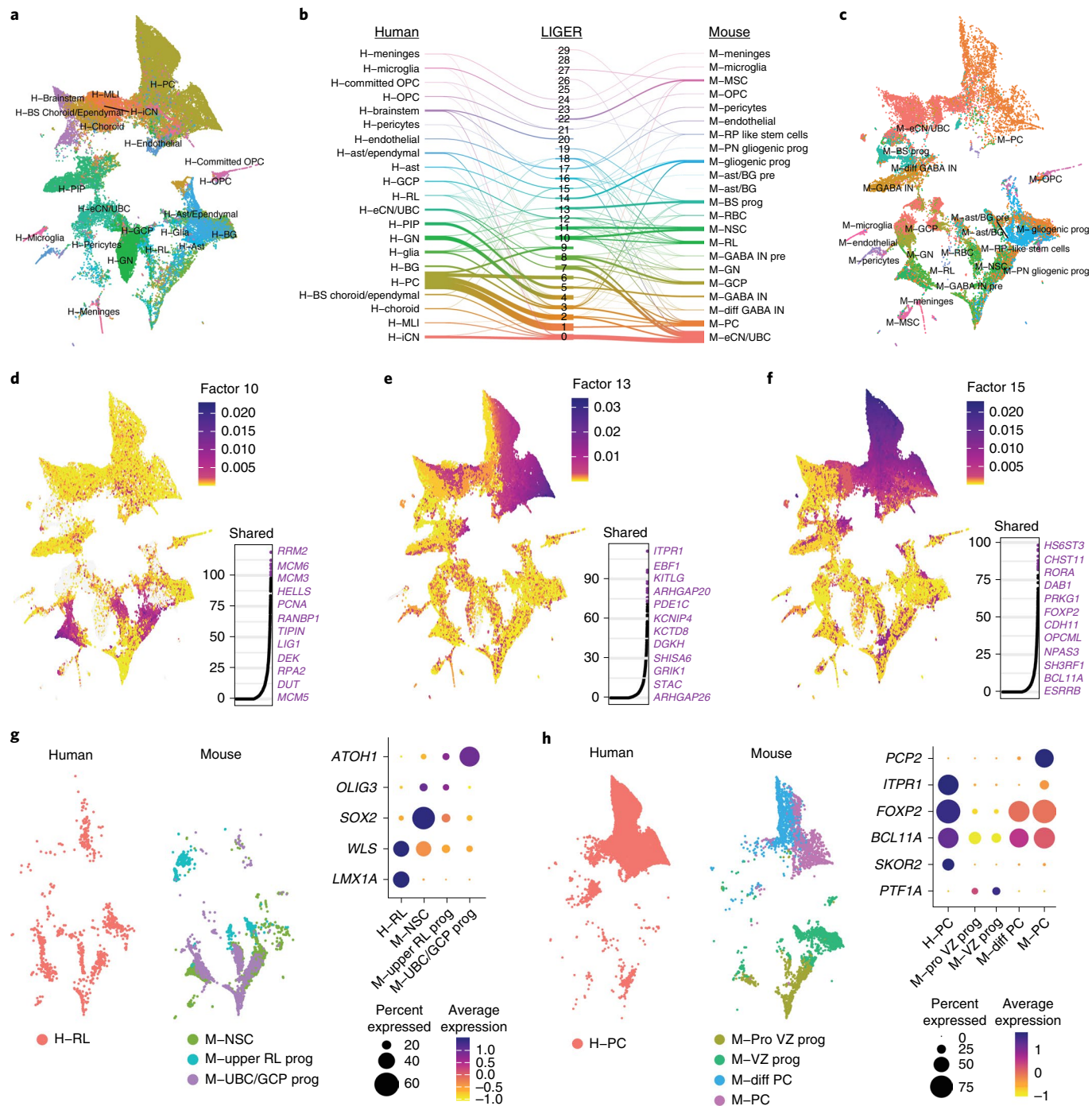


**Fig. 7 | Human-mouse cross-species analysis.** **a**, UMAP plot of nuclei from human cerebellum and cells from mouse cerebellum after LIGER analysis, showing only nuclei from human cerebellum ( $n=69,174$ ) and colored by cell type from the original analysis. **b**, River plot showing the relationship between original cluster assignments from our human cerebellum and a published mouse cerebellum dataset. **c**, UMAP plot of nuclei from human cerebellum and cells from mouse cerebellum after LIGER analysis, showing only cells from mouse cerebellum ( $n=39,130$ ) and colored by cell type from the original analysis. **d-f**, UMAP plots showing cell factor loading values and gene loading plots for factors corresponding to RL (d) and PC (e and f). **g**, UMAP plots show the human ( $n=1,018$ ) and mouse ( $n=7,034$ ) cell types contributing to factor 10. Dot plot shows expression of canonical RL genes delineated in human and mouse clusters. **h**, UMAP plots show the human and mouse PC clusters. Dot plot shows expression of canonical PC genes delineated in human and mouse PC clusters.

cell subtypes, we selected and subclustered nuclei in the Purkinje cell cluster and then used Monocle 3 (ref. <sup>27</sup>) to order them in pseudotime (Fig. 6). By labeling the cells by sample age, we detected a temporal progression (Fig. 6a). Plotting relative gene expression in pseudotime and then coloring cells by sample age demonstrated

little fluctuation in canonical Purkinje cell marker gene expression, with the exception of *CALB1* and *SKOR2* (Fig. 6b). *CALB1* was expressed at higher levels in later samples, whereas *SKOR2* expression declined with increasing gestational age. *RORA* was expressed throughout the Purkinje cell cluster, as were markers that, in mouse,

display parasagittal banding patterns of alternating Purkinje cells in mouse<sup>30</sup>, including *PLCB4* and *EBF2* (Fig. 6c). Few Purkinje cells expressed more mature markers, *ALDOC* and *PCP2*.

**Deconvolution of LCM and BrainSpan.** LCM is a technique used to harvest subpopulations of cells from precise anatomical regions of a heterogeneous tissue sample<sup>31,32</sup>. However, such samples can be contaminated with cell types in adjacent tissues. Therefore, we sought to directly investigate the cell type composition of our LCM samples by using the reference gene expression profiles from our snRNA-seq dataset. We used CIBERSORTx<sup>33</sup>, a machine learning method for inferring cell-type-specific gene expression profiles, to establish a transcriptional signature for each of the 21 cell types detected. This approach allowed us to estimate the relative proportions of each cell type present in every sample of our spatial transcriptional dataset. Overall, we found that the expected cell type had the highest relative abundance in each LCM sample (Extended Data Fig. 9). Cells corresponding to the RL (02-RL) cluster were most abundant in the LCM RL samples (median, 52%; range, 35–57%), whereas they represented only 7% of the cells in the EGL samples and were absent from PCL and bulk cerebellum samples. GCPs (03-GCP) were the most abundant cell type present in LCM EGL samples (median, 49%; range, 40–54%), whereas they represented only 6.5% of RL, 2% of PCL and 6% of bulk cerebellum. Purkinje cells (01-PC) were the most abundant cell type present in the LCM PCL samples (median, 43%; range, 32–57%), whereas they represented only 16% of bulk cerebellum and were absent from RL and EGL samples.

We also estimated the cell type composition of bulk cerebellar samples from BrainSpan using our fetal cerebellar transcriptional signatures. Overall, Purkinje cells were more abundant in bulk cerebellar samples from fetal development (Supplementary Fig. 4). Deconvolution using our fetal transcriptional signatures estimated that Purkinje cells made up a median of 23% in BrainSpan fetal samples and a median of 13% in postnatal samples. Endothelial cells (median, 21%; range, 15–55%), inhibitory cerebellar nuclei (iCNs) (median, 10%; range, 4–22%) and glia (median, 10%; range, 5–14%) were also detectable in BrainSpan fetal samples. However, several low-abundance cell types were not detectable (median, 0%) in most BrainSpan fetal samples, including RL, PIPs, Bergmann glia, oligodendrocyte progenitor cells (OPCs), microglia, meninges, pericytes, molecular layer interneurons, astrocytes and ependymal cells and choroid plexus.

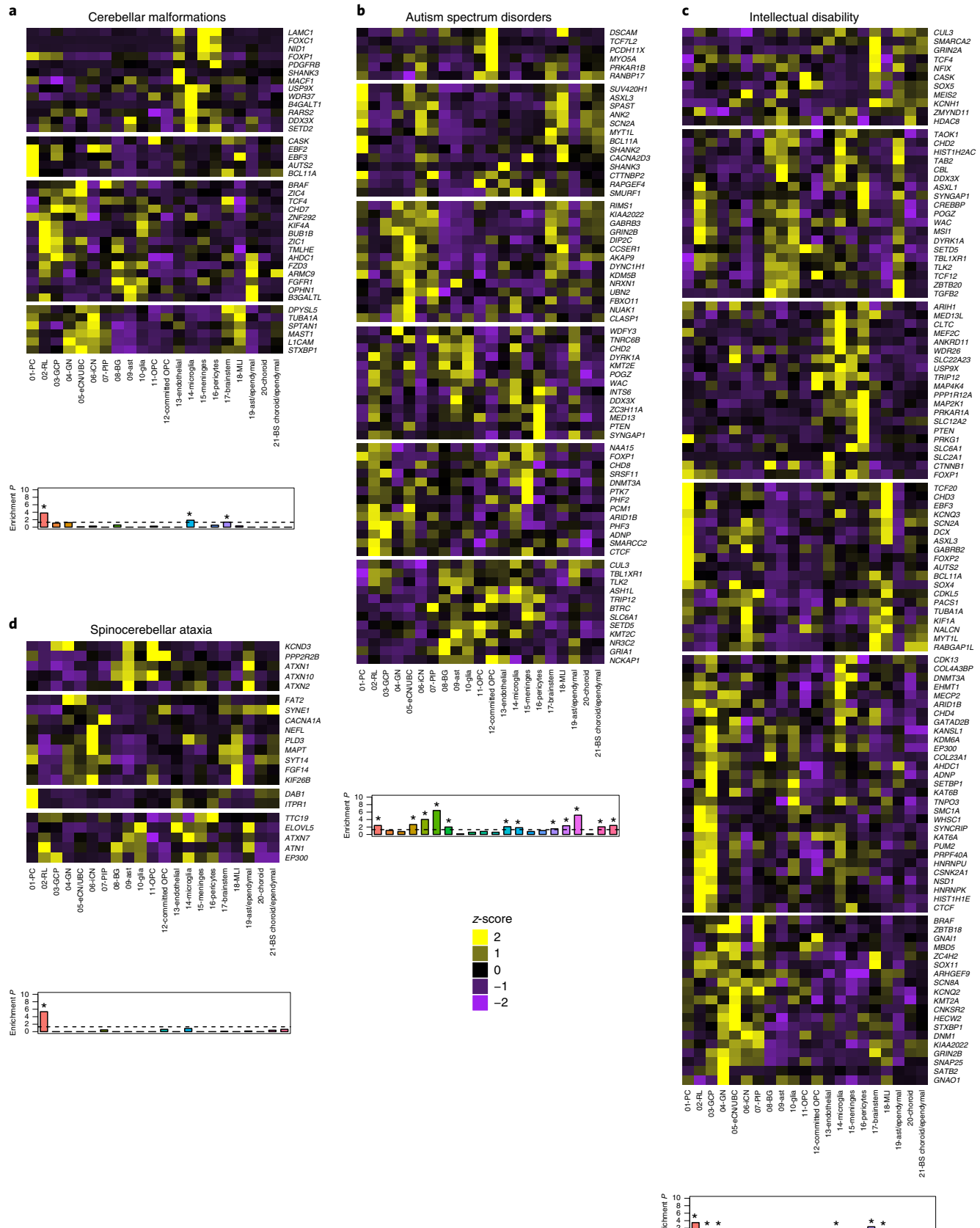
**Human–mouse cell type homology.** To examine conservation of cellular architecture in the developing cerebellum between human and mouse, we used LIGER<sup>34,35</sup> to align the transcriptomic cell types in our human fetal cerebellum with the cell types in a published dataset from the mouse developing cerebellum<sup>36</sup>. Overall, the joint analysis identified strong concordance between human and mouse cluster assignments for the individual datasets (Fig. 7). Shared metagene factors corresponded to the genes that define particular cell types in both species. First, we examined human RL metagenes. Factor 10 showed high loading values for *RRM2*, *PCNA* and

*LIG1*. These genes were enriched in DNA replication (hsa03030, FDR=1.04 × 10<sup>-12</sup>) and cell cycle (hsa04110, FDR=4.55 × 10<sup>-6</sup>) pathways consistent with their identity as neural progenitors. In mice, factor 10 corresponded to neural stem cells and GCP and UBC progenitors rather than to cells from the RL. Next, we examined human PC metagenes. Factors 13 and 15 showed high loading values for *ITPR1*, *EBF1* and *PDE1C* and *RORA*, *DAB1* and *FOXP2*, respectively, indicating that they were PC specific. Notably, ventricular zone progenitors that express *PTF1A* were present in the mouse data but not the human data. These factors corresponded to two subpopulations in mice: PC and differentiating PC.

**Cellular convergence of disease.** Cerebellar dysfunction underlies major childhood neurodevelopmental and adult-onset neurodegenerative disorders<sup>1,2</sup>. As a framework for understanding these complex disorders, we used our atlas of developing human cerebellum to identify the cell types in which mutations can act to cause pediatric and adult diseases (Fig. 8 and Supplementary Tables 11 and 12). We first examined the enrichment of genes implicated in structural cerebellar malformations, namely cerebellar hypoplasia and Dandy–Walker malformation, that are commonly diagnosed prenatally<sup>5,22</sup>. We found that 72% of genes associated with these common cerebellar malformations were expressed in the fetal cerebellum (Fig. 8a). These genes were significantly enriched in Purkinje cells, with prominent expression of *AUTS2*, *BCL11A*, *EBF2* and *EBF3*, endothelial cells (*MACF1* and *SHANK3*) and pericytes (*LAMC1*, *NID1* and *PDGFRB*). Next, we examined the enrichment of genes that cause Joubert syndrome (JS), a recessive neurodevelopmental ciliopathy defined by a distinctive hindbrain malformation<sup>37</sup>. None of the JS genes showed significant enrichment in cerebellar cell types (Extended Data Fig. 10a). Then, we examined the enrichment of high-confidence ASD risk genes<sup>38–42</sup>. Gene expression varied substantially across cell types, with significant enrichment of gene expression in multiple cell types: Purkinje cells, GNs, eCNs/UBCs, iCNs, PIPs, committed OPCs, endothelial cells, pericytes, brainstem, molecular layer interneurons (MLIs), choroid plexus and brainstem choroid plexus/ependymal cells (Fig. 8b). ASD genes were most prominently expressed in Purkinje cells (*ASXL3*, *BCL11A*, *CTTNBP2*, *SHANK2*, and *SUV420H1*), eCNs/UBCs (*CCSER1*, *DIP2C*, *FXBO11*, *NRXN1*, *NUAK1* and *PCM1*), committed OPCs (*DSCAM*, *MYO5A*, *NCKAP1*, *PCDH11X*, *PRKAR1B* and *TCF7L2*) and pericytes (*INTS6*, *MED13*, *PTEN*, *SMURF1*, *SYNGAP1* and *ZC3H11A*). We extended this analysis to examine high-confidence intellectual disability (ID) genes<sup>41</sup> and found prominent expression with significant enrichment in Purkinje cells (*ASXL3*, *AUTS2*, *BCL11A*, *CHD3*, *EBF3*, *FOXP2*, *GABRB2*, *PRKG1* and *TCF20*), RL (*ASXL1*, *CTCF*, *HIST1H1E*, *HNRNPK*, *HNRNPU*, *MSI1*, *NSD1*, *SMC1A*, *SYNCRI* and *WHSC1*), GCPs (*ADNP*, *CHD4*, *CSNK2A1*, *HNRNPK*, *HNRNPU*, *KAT6B*, *KDM6A*, *PRPF40A*, *SETBP1* and *SYNCRI*) and microglia (*ANKRD11*, *CLTC*, *COL4A3BP*, *EHMT1*, *HIST1H2AC*, *MECP2*, *MED13L*, *MEF2C*, *USP9X* and *WDR26*) (Fig. 8c). Lastly, we examined the expression of genes associated with two adult-onset neurodegenerative disorders: spinocerebellar ataxias (SCAs) and AD. SCAs are progressive disorders with

**Fig. 8 | Cerebellar cell type enrichment in pediatric and adult diseases. a–d,** Heat maps of mean expression per fetal cerebellar cell type for genes associated with pediatric (a, cerebellar malformations; b, ASDs; c, ID) or adult (d, SCA) diseases. Color scheme is based on z-score distribution. In the heat maps, each row represents one gene, and each column represents a single cell type. Gene expression was clustered by row. Horizontal white lines indicate branch divisions in row dendograms (not shown). The full list of genes is provided in Supplementary Table 11. Enrichment P values ( $-\log_{10} P$  value) for each cell type are shown in the bottom bar plots. Significance was determined by one-sample z-test, two-tailed P value. The dashed line is the significance threshold. Asterisk (\*) indicates significance ( $P < 0.05$ ) after Bonferroni correction: cerebellar malformations ( $P = 1.63 \times 10^{-4}$  for 01-PC;  $P = 0.01$  for 13-endothelial;  $P < 0.05$  for 16-pericytes), ASDs ( $P = 0.004$  for 01-PC;  $P = 0.002$  for 04-GN;  $P = 9.43 \times 10^{-5}$  for 05-eCN/UBC;  $P = 3.78 \times 10^{-7}$  for 06-iCN;  $P = 0.01$  for 07-PIP;  $P = 0.008$  for 12-committed OPC;  $P = 0.02$  for 13-endothelial;  $P = 0.03$  for 16-pericytes;  $P = 0.005$  for 17-brainstem;  $P = 6.74 \times 10^{-6}$  for 18-MLI;  $P = 0.009$  for 20-choroid; and  $P = 0.004$  for 21-BS choroid/ependymal), ID ( $P = 3.30 \times 10^{-4}$  for 01-PC;  $P = 0.02$  for 02-RL;  $P = 0.02$  for 03-GCP;  $P = 0.02$  for 13-endothelial;  $P = 0.004$  for 16-pericytes; and  $P = 0.04$  for 17-brainstem) and SCA ( $P = 4.56 \times 10^{-6}$  for 01-PC).

autosomal dominant inheritance that lead to irreversible Purkinje cell loss<sup>7</sup>. SCA genes were significantly enriched in Purkinje cells, driven by *DAB1* and *ITPR1* expression (Fig. 8d). AD is a progressive disease associated with age-related cognitive decline and aberrant neuron–glial interactions<sup>43</sup>. We examined the enrichment of AD risk genes identified in a recent case–control exome sequencing



study<sup>44</sup>. Although none of the AD genes showed significant enrichment in cerebellar cell types (Extended Data Fig. 10b), several genes were prominently expressed in microglia, consistent with emerging evidence<sup>6,43,44</sup>. Taken together, these findings demonstrate the value of our cerebellar developmental atlas as a rich resource for probing the cellular biology underlying complex disease.

## Discussion

By combining microdissection and single-nucleus capture methods, we provide a map of expression profiles for the major cell types present in the human cerebellum from 9 to 21 PCW. This ‘Developmental Cell Atlas of the Human Cerebellum’ provides molecular context for comparative evolution, benchmarking ex vivo model systems and investigating disease cell type origins.

The RL is a transient stem cell reservoir for glutamatergic neuron progenitors in the developing cerebellum<sup>24,25</sup>. We recently reported that the human RL is composed of an inner RL<sup>VZ</sup> and an outer RL<sup>SVZ</sup>, a feature that appears to be unique to humans and might explain the evolutionary expansion of the human cerebellum<sup>10</sup>. In this study, we performed both subcluster and trajectory analyses of the small recovered RL population to confirm that we can readily distinguish the RL<sup>VZ</sup> and outer RL<sup>SVZ</sup> compartments. In addition, we putatively identified the intermediate zone<sup>45</sup>, another transient progenitor region adjacent to the ventricular zone and the RL in early development, although this warrants further investigation given the few nuclei represented. Our human mouse comparisons indicate the human RL does not directly map onto the mouse RL. Additional cross-species analysis that retains spatial localization of the human and mouse RL is necessary.

During mid-gestation, the RL produces cells that migrate to become excitatory GNs in the EGL and UBCs, which are excitatory glutamatergic interneurons<sup>3</sup>. Additional eCNs are also generated from the RL, but their formation is completed before 8 PCW<sup>10</sup>. Distinguishing all of these closely related cell types is important because they have been implicated as the origin for group IV medulloblastoma, a poorly understood and aggressive subtype of childhood cerebellar tumor subtype<sup>36,46</sup>. Proliferative human RL<sup>SVZ</sup> progenitors are known to express both *LMX1A* and *EOMES*<sup>10</sup>. Although we recovered a cell population that expresses *LMX1A* and *EOMES*, this subset did not express the proliferative marker *MKI67*, leading us to identify this cluster as eCN/UBC. Although eCNs express *LMX1A* but not *EOMES*, UBCs express both *LMX1A* and *EOMES*. This cell cluster contained few nuclei (six total), and we were unable to discriminate eCNs and UBCs.

Neurogenesis in the VZ concludes between 8 and 10 PCW, whereas extensive migration of all VZ derivatives, including Purkinje cells and PIPs, occurs during early- and mid-fetal development<sup>29</sup>. In the mouse, Purkinje cell morphology and circuitry appears nearly identical; however, at late gestational stages, up to 50 molecularly heterogeneous Purkinje cell clusters, partly related to cell birthdates, are present<sup>47</sup>. These Purkinje cell clusters are subsequently transformed into longitudinal stripes along the mediolateral axis in a way that correlates with function<sup>30,48</sup>. In our dataset, Purkinje cells were the most frequent cell type recovered, but we did not readily detect Purkinje cell clusters with distinct transcriptional profiles. This is likely because Purkinje cell maturation begins during late gestation and peaks only after birth—once all GCPs in the EGL have differentiated and migrated inward to establish the internal granule layer. Consistently, expression of canonical mature Purkinje cell markers (*ALDOC* and *PCP2*) was low, whereas expression of early Purkinje cell differentiation marker<sup>49</sup> *SKOR2* declined with increasing gestational age, demonstrating that we recovered immature Purkinje cells in our dataset (Fig. 6c). Indeed, human Purkinje cells around 20 PCW display a nascent dendritic arbor, which expands considerably during late gestation and continues after birth<sup>29,50</sup>. Human–mouse comparisons reveal substantial

similarities in Purkinje cells across species. Additional sampling from earlier time points that capture more immature Purkinje cells and their progenitors, and from later time points that capture Purkinje cell maturation, are required to investigate differences in Purkinje cell trajectories between species.

Thus far, bulk RNA-seq data available from a limited number of fetal cerebellar samples have been reported<sup>15,16</sup>. Our data substantially augment previous work by providing three-fold more spatially resolved bulk transcriptional data and adding 70,000 single-nucleus transcriptomes. By directly comparing our spatial RNA-seq data with bulk RNA-seq data, we show that similarities are scarce; only one co-expression module from BrainSpan cerebellum correlated with our fetal EGL data. Bulk cerebellar data primarily emphasize Purkinje cells in prenatal samples and GNs in postnatal samples, obscuring detection of rare and transient cell types. We applied transcriptional signatures for cell types detected in our ‘Developmental Cell Atlas of the Human Cerebellum’ to infer cell type composition of our LCM and BrainSpan bulk cerebellum RNA-seq datasets. Our spatially captured data show a 40% abundance of the targeted cell type, with less than 20% abundances for other cell types (Extended Data Fig. 9). When we applied our fetal cell type signatures to the cerebellum data in BrainSpan, only half of the cell types identified in our snRNA-seq dataset were detected in the BrainSpan fetal samples (Supplementary Fig. 4). Notably, RL was one of the cell types that was not detectable in bulk cerebellum.

Human cerebellar development is protracted—extending from 30 d after conception through the second postnatal year of life—and is influenced by environmental and sensory cues that shape maturing brain circuitry<sup>4,50</sup>. The 17-week window of cerebellar development profiled here represents only a small slice of human cerebellar development. However, this time period instructs developmental processes that are fundamental for establishing the stereotypical lamination of the cerebellum that begins to emerge during this time<sup>4,10</sup>, and we found commonalities between humans and mice. Notably, we used our dataset to map genes associated with neurodevelopmental and adult-onset neurodegenerative disorders to relevant cell types. Although future studies are required to complete the cellular and transcriptional characterization of the human cerebellum across the complete human lifespan, our unique dataset serves as a framework with which to identify cell types, verify lineage relationships and establish the stoichiometry of cerebellar cell types across development.

## Online content

Any methods, additional references, Nature Research reporting summaries, source data, extended data, supplementary information, acknowledgements, peer review information; details of author contributions and competing interests; and statements of data and code availability are available at <https://doi.org/10.1038/s41593-021-00872-y>.

Received: 6 July 2020; Accepted: 10 May 2021;

Published online: 17 June 2021

## References

1. Sathyanaesan, A. et al. Emerging connections between cerebellar development, behaviour and complex brain disorders. *Nat. Rev. Neurosci.* **20**, 298–313 (2019).
2. Schmahmann, J. D. The cerebellum and cognition. *Neurosci. Lett.* **688**, 62–75 (2019).
3. Leto, K. et al. Consensus Paper: Cerebellar Development. *Cerebellum* **15**, 789–828 (2016).
4. Rakic, P. & Sidman, R. L. Histogenesis of cortical layers in human cerebellum, particularly the lamina dissecans. *J. Comp. Neurol.* **139**, 473–500 (1970).
5. Aldinger, K. A. & Doherty, D. The genetics of cerebellar malformations. *Semin. Fetal Neonatal Med.* **21**, 321–332 (2016).
6. Hoxha, E. et al. The emerging role of altered cerebellar synaptic processing in Alzheimer’s disease. *Front. Aging Neurosci.* **10**, 396 (2018).

7. Klockgether, T., Mariotti, C. & Paulson, H. L. Spinocerebellar ataxia. *Nat. Rev. Dis. Prim.* **5**, 24 (2019).
8. Corrales, J. D., Rocco, G. L., Blaess, S., Guo, Q. & Joyner, A. L. Spatial pattern of sonic hedgehog signaling through *Gli* genes during cerebellum development. *Development* **131**, 5581–5590 (2004).
9. Dahmane, N. & Ruiz i Altaba, A. Sonic hedgehog regulates the growth and patterning of the cerebellum. *Development* **126**, 3089–3100 (1999).
10. Haldipur, P. et al. Spatiotemporal expansion of primary progenitor zones in the developing human cerebellum. *Science* **366**, 454–460 (2019).
11. Holgado, B. L., Guerreiro Stucklin, A., Garzia, L., Daniels, C. & Taylor, M. D. Tailoring medulloblastoma treatment through genomics: making a change, one subgroup at a time. *Annu. Rev. Genomics Hum. Genet.* **18**, 143–166 (2017).
12. Volpe, J. J. Cerebellum of the premature infant: rapidly developing, vulnerable, clinically important. *J. Child Neurol.* **24**, 1085–1104 (2009).
13. Johnson, M. B. et al. Functional and evolutionary insights into human brain development through global transcriptome analysis. *Neuron* **62**, 494–509 (2009).
14. Kang, H. J. et al. Spatio-temporal transcriptome of the human brain. *Nature* **478**, 483–489 (2011).
15. Li, M. et al. Integrative functional genomic analysis of human brain development and neuropsychiatric risks. *Science* **362**, eaat7615 (2018).
16. Miller, J. A. et al. Transcriptional landscape of the prenatal human brain. *Nature* **508**, 199–206 (2014).
17. Mu, Q., Chen, Y. & Wang, J. Deciphering brain complexity using single-cell sequencing. *Genomics Proteomics Bioinformatics* **17**, 344–366 (2019).
18. Rosenberg, A. B. et al. Single-cell profiling of the developing mouse brain and spinal cord with split-pool barcoding. *Science* **360**, 176–182 (2018).
19. Zhang, B. & Horvath, S. A general framework for weighted gene co-expression network analysis. *Stat. Appl. Genet. Mol. Biol.* **4**, Article17 (2005).
20. Lange, W. Cell number and cell density in the cerebellar cortex of man and some other mammals. *Cell Tissue Res.* **157**, 115–124 (1975).
21. McGinnis, C. S., Murrow, L. M. & Gartner, Z. J. DoubletFinder: doublet detection in single-cell RNA sequencing data using artificial nearest neighbors. *Cell Syst.* **8**, 329–337 (2019).
22. Aldinger, K. A. et al. Redefining the etiologic landscape of cerebellar malformations. *Am. J. Hum. Genet.* **105**, 606–615 (2019).
23. Butler, A., Hoffman, P., Smibert, P., Papalexi, E. & Satija, R. Integrating single-cell transcriptomic data across different conditions, technologies, and species. *Nat. Biotechnol.* **36**, 411–420 (2018).
24. Machold, R. & Fishell, G. *Math1* is expressed in temporally discrete pools of cerebellar rhombic-lip neural progenitors. *Neuron* **48**, 17–24 (2005).
25. Wang, V. Y., Rose, M. F. & Zoghbi, H. Y. *Math1* expression redefines the rhombic lip derivatives and reveals novel lineages within the brainstem and cerebellum. *Neuron* **48**, 31–43 (2005).
26. Englund, C. et al. Unipolar brush cells of the cerebellum are produced in the rhombic lip and migrate through developing white matter. *J. Neurosci.* **26**, 9184–9195 (2006).
27. Cao, J. et al. The single-cell transcriptional landscape of mammalian organogenesis. *Nature* **566**, 496–502 (2019).
28. Fink, A. J. et al. Development of the deep cerebellar nuclei: transcription factors and cell migration from the rhombic lip. *J. Neurosci.* **26**, 3066–3076 (2006).
29. Zecevic, N. & Rakic, P. Differentiation of Purkinje cells and their relationship to other components of developing cerebellar cortex in man. *J. Comp. Neurol.* **167**, 27–47 (1976).
30. Dastjerdi, F. V., Consalez, G. G. & Hawkes, R. Pattern formation during development of the embryonic cerebellum. *Front. Neuroanat.* **6**, 10 (2012).
31. Emmert-Buck, M. R. et al. Laser capture microdissection. *Science* **274**, 998–1001 (1996).
32. Espina, V. et al. Laser-capture microdissection. *Nat. Protoc.* **1**, 586–603 (2006).
33. Newman, A. M. et al. Determining cell type abundance and expression from bulk tissues with digital cytometry. *Nat. Biotechnol.* **37**, 773–782 (2019).
34. Liu, J. et al. Jointly defining cell types from multiple single-cell datasets using LIGER. *Nat. Protoc.* **15**, 3632–3662 (2020).
35. Welch, J. D. et al. Single-cell multi-omic integration compares and contrasts features of brain cell identity. *Cell* **177**, 1873–1887 (2019).
36. Vladouli, M. C. et al. Childhood cerebellar tumours mirror conserved fetal transcriptional programs. *Nature* **572**, 67–73 (2019).
37. Van De Weghe, J. C. et al. Mutations in ARMC9, which encodes a basal body protein, cause Joubert syndrome in humans and ciliopathy phenotypes in zebrafish. *Am. J. Hum. Genet.* **101**, 23–36 (2017).
38. Feliciano, P. et al. Exome sequencing of 457 autism families recruited online provides evidence for autism risk genes. *NPJ Genom. Med.* **4**, 19 (2019).
39. RK, C. Y. et al. Whole genome sequencing resource identifies 18 new candidate genes for autism spectrum disorder. *Nat. Neurosci.* **20**, 602–611 (2017).
40. Ruzzo, E. K. et al. Inherited and de novo genetic risk for autism impacts shared networks. *Cell* **178**, 850–866 (2019).
41. Willsey, A. J. et al. The Psychiatric Cell Map Initiative: a convergent systems biological approach to illuminating key molecular pathways in neuropsychiatric disorders. *Cell* **174**, 505–520 (2018).
42. Yuen, R. K. et al. Whole-genome sequencing of quartet families with autism spectrum disorder. *Nat. Med.* **21**, 185–191 (2015).
43. De Strooper, B. & Karlan, E. The cellular phase of Alzheimer's disease. *Cell* **164**, 603–615 (2016).
44. Bis, J. C. et al. Whole exome sequencing study identifies novel rare and common Alzheimer's-Associated variants involved in immune response and transcriptional regulation. *Mol. Psychiatry* **25**, 1859–1875 (2018).
45. Wizeman, J. W., Guo, Q., Wilion, E. M. & Li, J. Y. Specification of diverse cell types during early neurogenesis of the mouse cerebellum. *eLife* **8**, e42388 (2019).
46. Hovestadt, V. et al. Resolving medulloblastoma cellular architecture by single-cell genomics. *Nature* **572**, 74–79 (2019).
47. Carter, R. A. et al. A single-cell transcriptional atlas of the developing murine cerebellum. *Curr. Biol.* **28**, 2910–2920 (2018).
48. Sillitoe, R. V. & Joyner, A. L. Morphology, molecular codes, and circuitry produce the three-dimensional complexity of the cerebellum. *Annu. Rev. Cell Dev. Biol.* **23**, 549–577 (2007).
49. Nakatani, T., Minaki, Y., Kumai, M., Nitta, C. & Ono, Y. The c-Ski family member and transcriptional regulator Corl2/Skor2 promotes early differentiation of cerebellar Purkinje cells. *Dev. Biol.* **388**, 68–80 (2014).
50. Haldipur, P. et al. Preterm delivery disrupts the developmental program of the cerebellum. *PLoS ONE* **6**, e23449 (2011).

**Publisher's note** Springer Nature remains neutral with regard to jurisdictional claims in published maps and institutional affiliations.

© The Author(s), under exclusive licence to Springer Nature America, Inc. 2021

## Methods

**Cerebellum samples.** Acquisition of human tissue samples was approved by the Seattle Children's Hospital (SCH) Institutional Review Board. Experiments were performed in accordance with SCH ethical and legal guidelines. Specimens from fetal (9–21 PCW) human cerebellum were obtained from the Birth Defects Research Laboratory at the University of Washington or the Joint MRC/Wellcome (MR/R006237/1) Human Developmental Biology Resource<sup>51</sup> (<https://www.hdb.org/>) with ethics board approval and maternal written consent obtained before specimen collection.

**Histology, immunohistochemistry and in situ hybridization analyses.** Fixation, tissue processing and immunohistochemistry were performed as previously described<sup>50</sup> using the following primary antibodies: calbindin (swant, CB38, rabbit, 1:3,000), PAX6 (BioLegend, 901301, rabbit, 1:300), SKOR2 (Novus Biologicals, NBP2-14565, rabbit, 1:100) and NEUN (Millipore, MAB377, mouse, 1:100). All sections were counterstained using VECTASHIELD DAPI (H1000, Vector Labs), which marks all nuclei.

In situ hybridization was performed using commercially available probes from Advanced Cell Diagnostics. Manufacturer-recommended protocols available on the Advanced Cell Diagnostics website were used without modification. Probes used included *LMX1A* (no. 540661), *MKI67* (no. 591771), *ATOH1* (no. 417861), *OTX2* (no. 484581) and *HOXB3* (custom made). All sections were counterstained using Fast Green.

Slides processed for fluorescent immunohistochemistry were imaged using a Zeiss LSM Meta confocal microscope and ZEN 2009 software (Zeiss). Bright-field imaging was performed using a NanoZoomer digital pathology slide scanner (Hamamatsu). Barring minor adjustments limited to contrast and brightness to the entire image, no additional image alteration was performed.

**LCM.** Whole cerebellum was dissected from 16 fetal specimens that had intact calvaria to ensure correct orientation of the cerebellum. Intact cerebella were embedded in OCT, frozen at  $-80^{\circ}\text{C}$  and cryosectioned at 16  $\mu\text{m}$  in the sagittal plane through the cerebellar vermis onto PEN Membrane Glass Slides (Applied Biosystems). Total RNA was isolated from one whole section using the Qiagen RNeasy Micro Kit, and RNA quality was assessed using the Agilent Bioanalyzer 6000 Pico Kit before proceeding with LCM. LCM was performed using the Leica DM LMD-6000 Laser Microdissection system to capture tissue containing PCL and EGL from each of 6–8 sections per slide into separate collection tubes. Total RNA was then isolated from LCM-enriched samples pooled across nine slides using the Qiagen RNeasy Micro Kit. LCM was previously performed to capture RL<sup>VZ</sup> and RL<sup>SVZ</sup>, and then total RNA was isolated from RL<sup>VZ</sup> and RL<sup>SVZ</sup>, resulting in two RNA samples per specimen<sup>10</sup>.

**RNA-seq and analysis.** Sequencing libraries were prepared using the Illumina TruSeq RNA Access Prep Kit and 25 ng of total RNA per sample, according to the manufacturer's protocol. RNA libraries were barcoded and sequenced including 6–8 samples per lane on an Illumina HiSeq 2000. FASTQ files for RL<sup>VZ</sup> and RL<sup>SVZ</sup> samples from the same specimen (phs001908.v1.p1) were merged to generate the RL dataset and analyzed together with data for the other samples. Paired-end reads (100 bp) were aligned to the human reference genome (NCBI build 37/hg19) using STAR<sup>52</sup>; gene counts were summarized using HTSeq<sup>53</sup>; and gene-level differential expression was analyzed using DESeq2 (ref. <sup>54</sup>) specifying ~ batch + age + region as the experimental design. Six samples were deemed to be outliers because PCA separated these samples from all others; these samples were removed from additional analyses. Sample sex was confirmed by comparing expression of the female-specific non-coding RNA *XIST* and the chromosome Y-specific gene *DDX3Y*. Significant results are reported as Benjamini–Hochberg-adjusted *P* values. Pathway enrichment was performed using String version 11.0 (ref. <sup>55</sup>).

**Gene co-expression network analyses.** WGCNA was performed using the R package<sup>19</sup>. Summarized gene counts were converted to reads per kilobase of transcript per million mapped reads (RPKM) using RNA-SeQC<sup>56</sup> version 1.1.8. log<sub>2</sub>-transformed RPKM values were used for this analysis, as described previously<sup>15</sup>.

**BrainSpan RNA-seq data.** Gene-level expression data in counts and RPKM for the BrainSpan RNA-seq dataset generated from postmortem human brain were downloaded (<http://www.development.psychencode.org>). We restricted our analysis to the cerebellum, selecting data from 35 individuals and including three brain regions: CBC (cerebellar cortex), CB (cerebellum) and URL (upper rhombic lip).

**SPLiT-seq method.** Specimens were flash-frozen in liquid nitrogen and stored at  $-80^{\circ}\text{C}$  until use. Frozen tissue samples (whole or half cerebellum) were pulverized on dry ice using a ceramic mortar and pestle. Pulverized samples were transferred to chilled microcentrifuge tubes and stored at  $-80^{\circ}\text{C}$  until use. Nuclei were isolated from either 150 mg of pulverized tissue or an entire amount of dissected cerebellum using a published protocol<sup>57</sup>. Nuclei were fixed according to the SPLiT-seq protocol<sup>18</sup>. The SPLiT-seq method was performed in an initial experiment as previously described (experiment 1)<sup>22</sup>. Two additional SPLiT-seq

experiments were performed using nuclei isolated from 13 cerebellar specimens using the published detailed experimental protocol<sup>18</sup>. Libraries were first sequenced on an Illumina NextSeq using 150-nucleotide kits and paired-end sequencing. Libraries were then sequenced on an Illumina NovaSeq S2 flow cell by SeqMatic (experiment 2) or the Northwest Genomics Center at the University of Washington (experiment 3). We used the SPLiT-seq pipeline to convert FASTQ files into digital gene expression matrices from each sequencing run: <https://github.com/yjzhang/split-seq-pipeline>.

**snRNA-seq analysis.** Deep and shallow sequencing runs from experiment 1 (ref. <sup>23</sup>) and shallow sequencing runs from experiment 2 and experiment 3 were filtered independently (datasets 1,000, 5,000, 10,000 and 80,000, respectively). Nuclei with fewer than 200 genes, more than 4 standard deviations above the median number of genes or UMIs or more than 1–5% mitochondrial genes were removed from the analysis (Supplementary Table 7). DoubletFinder<sup>21</sup> was used to detect likely doublets, assuming a rate of 5%, which were discarded from analysis. Sample sex was confirmed by counting reads mapped to the female-specific non-coding RNA *XIST* and the chromosome Y-specific gene *DDX3Y*. We used Seurat version 3 (ref. <sup>23</sup>) for downstream analysis. The four filtered datasets (1,000, 5,000, 10,000 and 80,000) were combined into a single dataset using canonical correlation analysis with anchors ('FindIntegrationAnchors') to correct for batch effects<sup>58</sup>. The top 2,000 most variable genes were used to find individual cells in each sequencing run that originate from the same biological state, which became the anchors to merge runs together. The resulting dataset was then scaled and centered as well as regressed out cell cycle difference (S.score – G2M.score). Data dimensionality of the integrated dataset was reduced by PCA ('RunPCA'), then UMAP ('RunUMAP'), then shared nearest neighbor graph construction ('FindNeighbors') and, finally, Louvain clustering ('FindClusters'), using the first 75 PCs and a resolution of 1.5 to determine cluster assignment. A Wilcoxon rank-sum test was performed to identify differentially expressed genes for each cluster ('FindAllMarkers') and compare them to known gene markers for cell type assignment. One cluster with no significant differentially expressed genes and another cluster with an enrichment of mitochondrial genes were removed.

Subcluster analysis was performed by subsetting populations of interest from the overall dataset. Clustering and differential gene tests were repeated with a subpopulation-specific number of PCs determined by 'ElbowPlot'. Then, pseudotime analysis was performed using Monocle 3 (ref. <sup>27</sup>). Subsets were normalized ('preprocess\_cds'), and dimension reduction was applied ('reduce\_dimension'), followed by clustering ('cluster\_cells') and visualization ('learn\_graph'). Pseudotemporal ordering of cells was performed ('order\_cells') by selecting a biologically relevant starting point. Genes of interest were used to construct the pseudotime trajectory ('plot\_genes\_in\_pseudotime').

**Cell type deconvolution.** We used CIBERSORTx<sup>33</sup> to estimate the cell type composition in the LCM-isolated and BrainSpan RNA-seq samples. We downsampled our integrated snRNA-seq dataset to 100 cells per cell type, built a cell type signature matrix with this digital expression matrix and imputed cell fractions for each of the 57 LCM RNA-seq samples and 35 BrainSpan cerebellar samples.

**Cross-species analysis.** To analyze the developing cerebellum between human and mouse, we selected high-confidence human-to-mouse (one-to-one) orthologs from Ensembl release 101 (<http://www.ensembl.org/biomart/martview>). We downloaded single-cell RNA-seq data from nine cerebellum samples across mouse embryonic and postnatal development from the Gene Expression Omnibus (GSE118068)<sup>36</sup> and restricted our analysis to the most relevant period (E10, E12, E14, E16, E18 or P0). We selected the union of orthologs present in our human dataset and in the downloaded mouse dataset (13,182 genes) and then used LIGER<sup>34,35</sup> to integrate the filtered datasets and identify shared cell types in the cerebellum across these two species. Variable gene selection, normalization and scaling of individual genes were performed on the combined dataset using integrative non-negative matrix factorization with  $k = 20$  to define dataset-specific and shared metagenes, which correspond to genes that define particular cell types.

**Gene set curation.** Disease gene lists are provided in Supplementary Table 11. The cerebellar malformation gene list was obtained from exome sequencing analysis and published Dandy–Walker malformation and cerebellar hypoplasia genes<sup>5,22,59</sup>. The cerebellar malformation (CBLM) list included 54 genes. The JS gene list was compiled from published JS genes<sup>37,60–62</sup>. The JS list included 42 genes. The ASD gene set was compiled by selecting high-confidence ASD genes identified through exome and genome sequencing<sup>38–42,63</sup>. The final ASD list included 108 genes. The ID gene list was compiled by selecting genes identified through exome sequencing<sup>11,64,65</sup>. The final ID list included 186 genes. The SCA gene set was compiled by selecting genes from OMIM phenotype PS164400. The SCA list included 44 genes. The AD gene list was compiled by selecting genes identified through exome sequencing<sup>44</sup>. The Alzheimer's disease (ALZ) list included 120 genes.

**Cell type enrichment analysis.** We used a one-sample *z*-test<sup>66</sup> to identify cell types that showed enriched gene expression associated with particular gene sets. We

calculated the average expression for each gene per cell type and then removed genes with expression values less than 1 for more than one cell type to define a population size of 4,457 genes (Supplementary Table 12). Enrichment *P* values were corrected for multiple testing using the Bonferroni method.

**Statistical tests.** No statistical methods were used to predetermine sample sizes. No randomization was used in this study. Distributions of the data were not tested. Statistical tests were performed using R version 3.3.3 and RStudio version 1.0.143. The Wald test was used to calculate differential gene expression, and *P* values were adjusted using the FDR approach within DESeq2 (ref. <sup>54</sup>). A loess regression was used to estimate gene expression across time. Fisher's exact test was used for Gene Ontology, pathway and WGCNA module enrichment. The Wilcoxon rank-sum test was used to calculate cluster markers within Seurat<sup>23</sup>. Three independent snRNA-seq experiments were performed. Gene set enrichment analysis was performed using a one-sided *z*-test, and *P* values were adjusted using the Bonferroni method.

**Reporting Summary.** Further information on research design is available in the Nature Research Reporting Summary linked to this article.

## Data availability

Processed data are available through the Human Cell Atlas (<https://www.covid19cellatlas.org/alddinger20>), the UCSC Cell Browser (<https://cbl-dev.cells.ucsc.edu>) and upon request. Sequence data were deposited into the Database of Genotypes and Phenotypes, under accession number phs001908.v2.p1, and are available upon request.

## Code availability

No custom code was used in this study. Open-source algorithms were used as detailed in analysis methods. Details on how these algorithms were used are available from the corresponding author upon request.

## References

51. Gerrelli, D., Lisgo, S., Copp, A. J. & Lindsay, S. Enabling research with human embryonic and fetal tissue resources. *Development* **142**, 3073–3076 (2015).
52. Dobin, A. et al. STAR: ultrafast universal RNA-seq aligner. *Bioinformatics* **29**, 15–21 (2013).
53. Anders, S., Pyl, P. T. & Huber, W. HTSeq—a Python framework to work with high-throughput sequencing data. *Bioinformatics* **31**, 166–169 (2015).
54. Love, M. I., Huber, W. & Anders, S. Moderated estimation of fold change and dispersion for RNA-seq data with DESeq2. *Genome Biol.* **15**, 550 (2014).
55. Szklarczyk, D. et al. STRING v11: protein–protein association networks with increased coverage, supporting functional discovery in genome-wide experimental datasets. *Nucleic Acids Res.* **47**, D607–D613 (2019).
56. DeLuca, D. S. et al. RNA-SeQC: RNA-seq metrics for quality control and process optimization. *Bioinformatics* **28**, 1530–1532 (2012).
57. Hodge, R. D. et al. Conserved cell types with divergent features in human versus mouse cortex. *Nature* **573**, 61–68 (2019).
58. Stuart, T. et al. Comprehensive integration of single-cell data. *Cell* **177**, 1888–1902 (2019).
59. Mirzaa, G. M. et al. De novo and inherited variants in ZNF292 underlie a neurodevelopmental disorder with features of autism spectrum disorder. *Genet. Med.* **22**, 538–546 (2020).
60. Epting, D. et al. Loss of CBY1 results in a ciliopathy characterized by features of Joubert syndrome. *Hum. Mutat.* **41**, 2179–2194 (2020).
61. Latour, B. L. et al. Dysfunction of the ciliary ARMC9/TOGARAM1 protein module causes Joubert syndrome. *J. Clin. Invest.* **130**, 4423–4439 (2020).
62. Luo, M. et al. Disrupted intraflagellar transport due to *IFT74* variants causes Joubert syndrome. *Genet. Med.* <https://doi.org/10.1038/s41436-021-01106-z> (2021).
63. Sanders, S. J. et al. Insights into autism spectrum disorder genomic architecture and biology from 71 risk loci. *Neuron* **87**, 1215–1233 (2015).
64. Deciphering Developmental Disorders Study. Prevalence and architecture of de novo mutations in developmental disorders. *Nature* **542**, 433–438 (2017).
65. Rauch, A. et al. Range of genetic mutations associated with severe non-syndromic sporadic intellectual disability: an exome sequencing study. *Lancet* **380**, 1674–1682 (2012).
66. Irizarry, R. A., Wang, C., Zhou, Y. & Speed, T. P. Gene set enrichment analysis made simple. *Stat. Methods Med. Res.* **18**, 565–575 (2009).

## Acknowledgements

This study was funded by the National Institutes of Health under National Institute of Neurological Disorders and Stroke, National Institute of Child Health and Human Development and National Institute of Mental Health grant numbers NS095733 to K.J.M., HD000836 to I.A.G., NS050375 to W.B.D. and MH110926, MH116488 and MH106934 to N.S. The project that gave rise to these results received the support of a fellowship from 'la Caixa' Foundation (ID 100010434) to G. Santpere. The fellowship code is LCF/BQ/PI19/11690010. K.A.A. received a Parental Leave Grant from Life Science Editors and would like to thank C. Lilliehook for editorial assistance. This publication is part of the Human Cell Atlas ([www.humanzellatlas.org/publications](http://www.humanzellatlas.org/publications)).

## Author contributions

K.A.A. conceived the project, designed experiments, analyzed data and wrote the manuscript. Z.T. performed experiments, analyzed data and contributed to manuscript preparation. I.G.P. analyzed data and contributed to manuscript preparation. P.H. performed experiments and contributed to data interpretation and manuscript preparation. M.D., M.H. and L.M.O. performed experiments. M.H., C.R., A.B.R. and G. Seelig provided SPLiT-seq expertise and experimental support. I.G.P., A.E.T., G. Santpere and B.L.G. analyzed data. F.O.G., D.O. and P.A. provided experimental and/or analysis support. S.N.L., N.S., W.B.D., D.D. and I.A.G. supervised experiments and/or data analysis. K.J.M. provided general oversight and contributed to data interpretation and manuscript preparation.

## Competing interests

C.R., A.B.R. and G. Seelig are shareholders of Parse Biosciences. The remaining authors declare no competing financial interests.

## Additional information

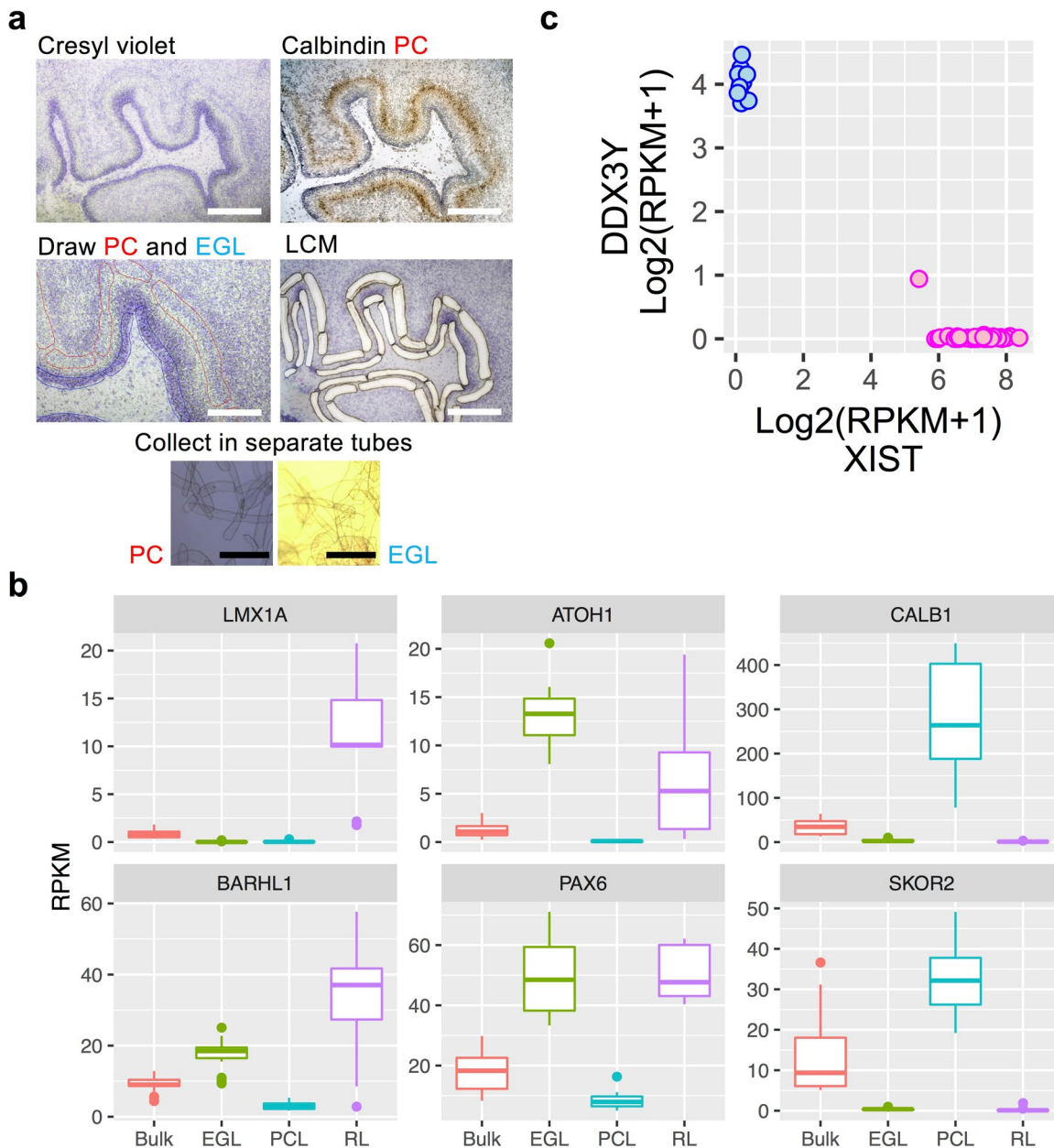
**Extended data** is available for this paper at <https://doi.org/10.1038/s41593-021-00872-y>.

**Supplementary information** The online version contains supplementary material available at <https://doi.org/10.1038/s41593-021-00872-y>.

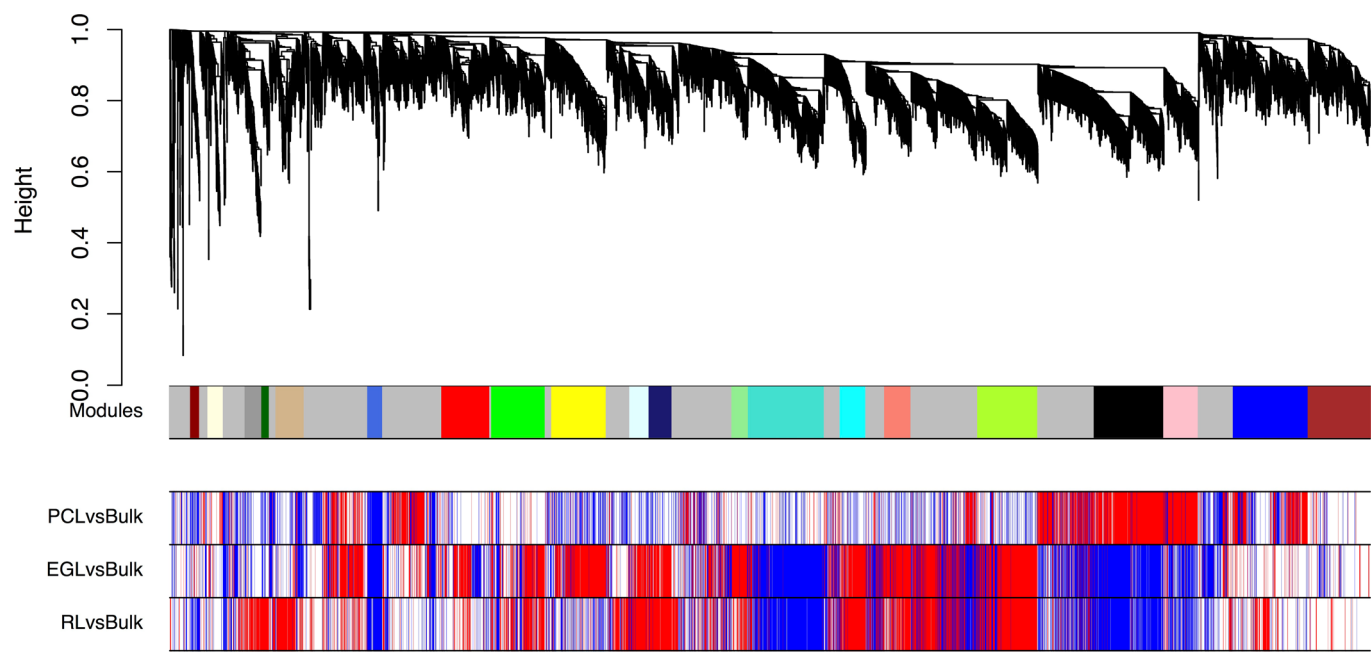
**Correspondence and requests for materials** should be addressed to K.A.A. or K.J.M.

**Peer review information** *Nature Neuroscience* thanks Mary Hatten, Fenna Krienen, and the other, anonymous, reviewer(s) for their contribution to the peer review of this work.

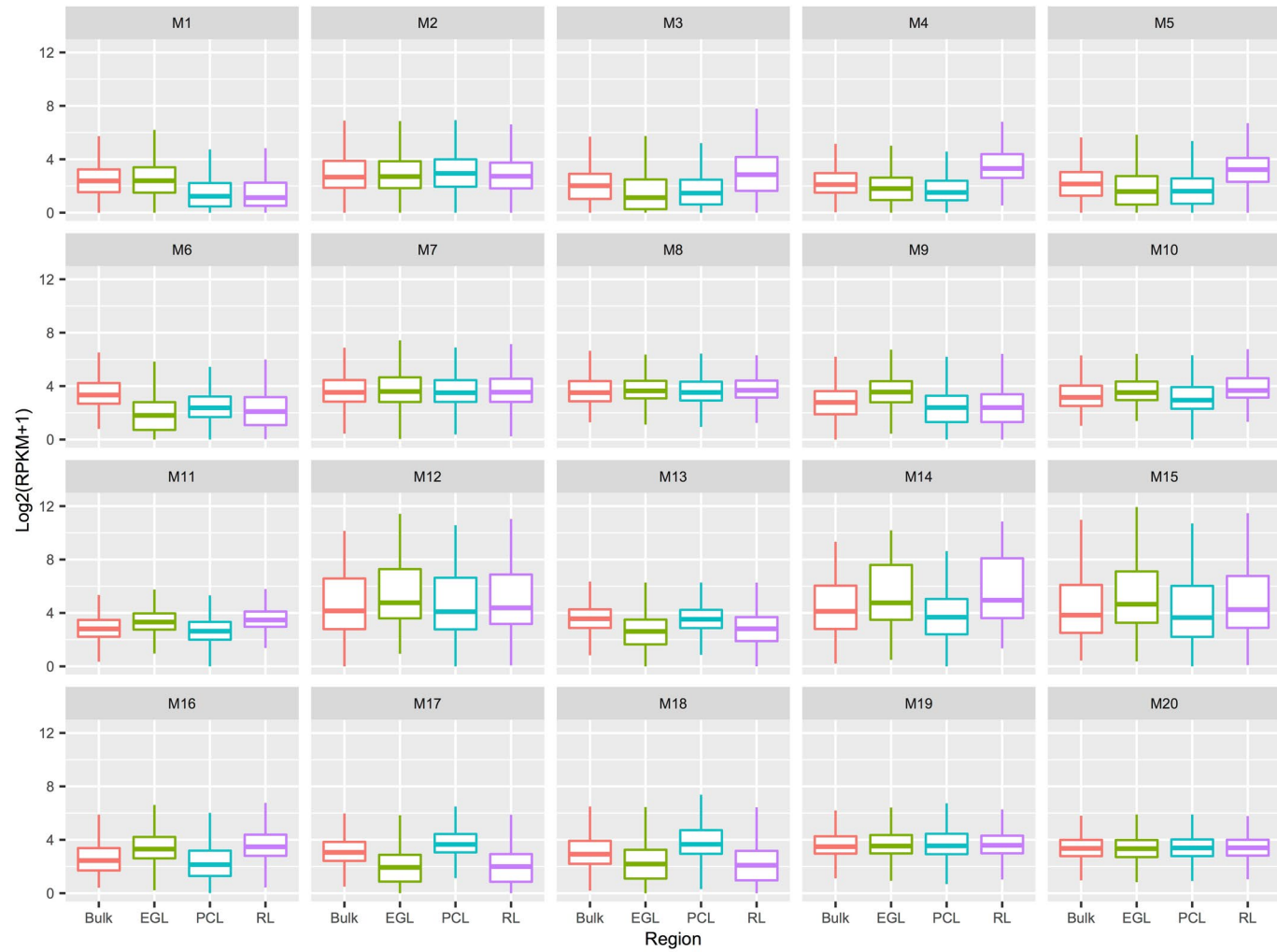
**Reprints and permissions information** is available at [www.nature.com/reprints](http://www.nature.com/reprints).



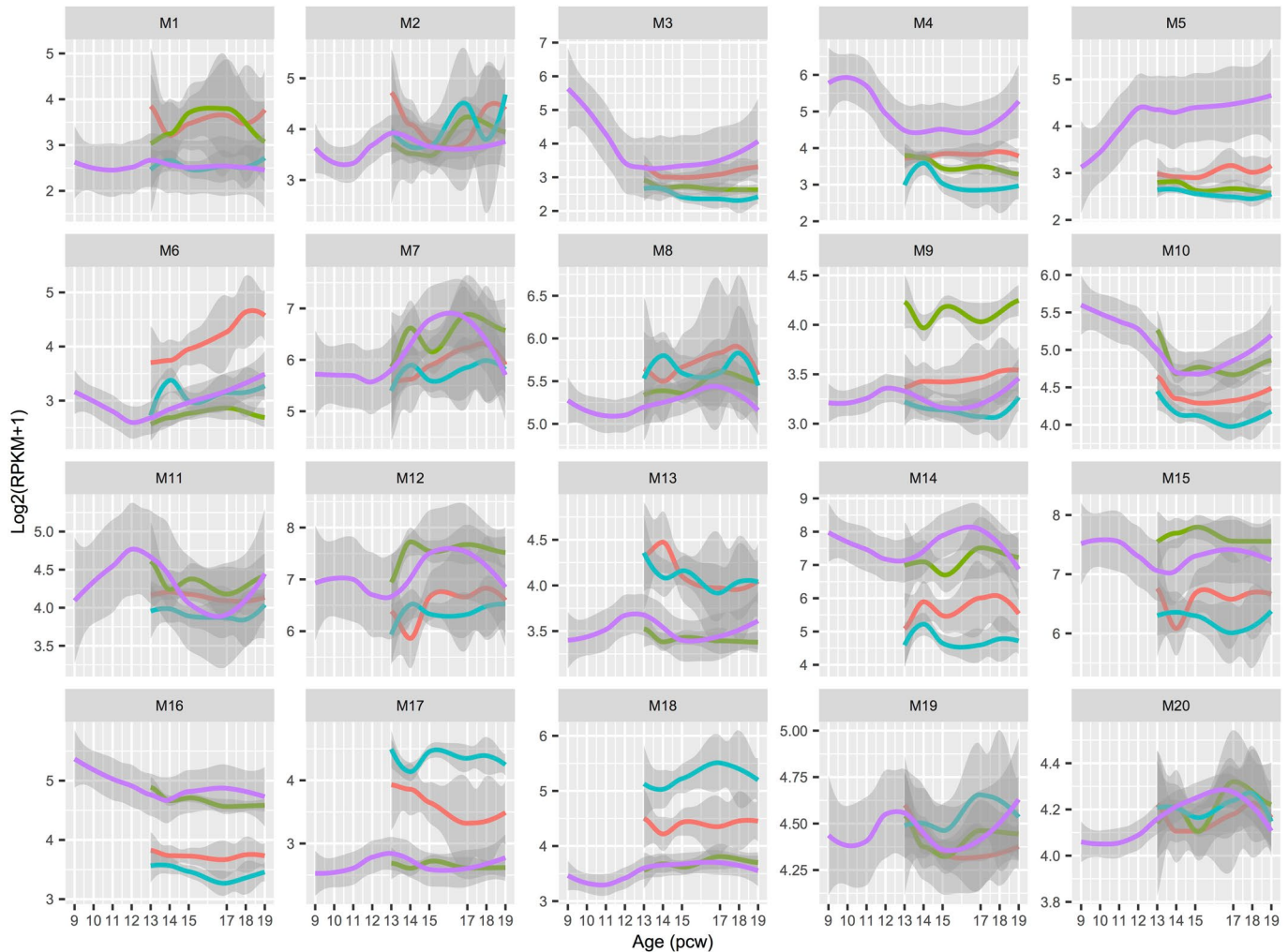
**Extended Data Fig. 1 | Quality control related analyses of LCM RNA-seq data.** **a**, Example of cerebellum section stained with cresyl violet (purple) and anti-calbindin antibody (brown). Section before and after LCM and images of Purkinje cell (PC) and external granule cell layer (EGL) tissue captured into collection tubes are shown. Example shown is representative of 11 specimens. Scale bars: 200  $\mu$ m (white), 400  $\mu$ m (black). **b**, Boxplots of gene expression for established markers showing highest expression in the expected samples (box: 25–75<sup>th</sup> percentiles, whiskers: 10–90<sup>th</sup> percentiles, horizontal line in box: median). Dots indicate outliers. RNA-seq sample numbers per region: n=13 for bulk; 17 for EGL; 18 for PCL; 9 for RL. **c**, Expression of the female-specific non-coding RNA *XIST* and the chromosome Y specific gene *DDX3Y* show correct sex assignment for female (pink) and male (blue) samples. RNA-seq sample numbers per sex: n=44 female; 13 male.



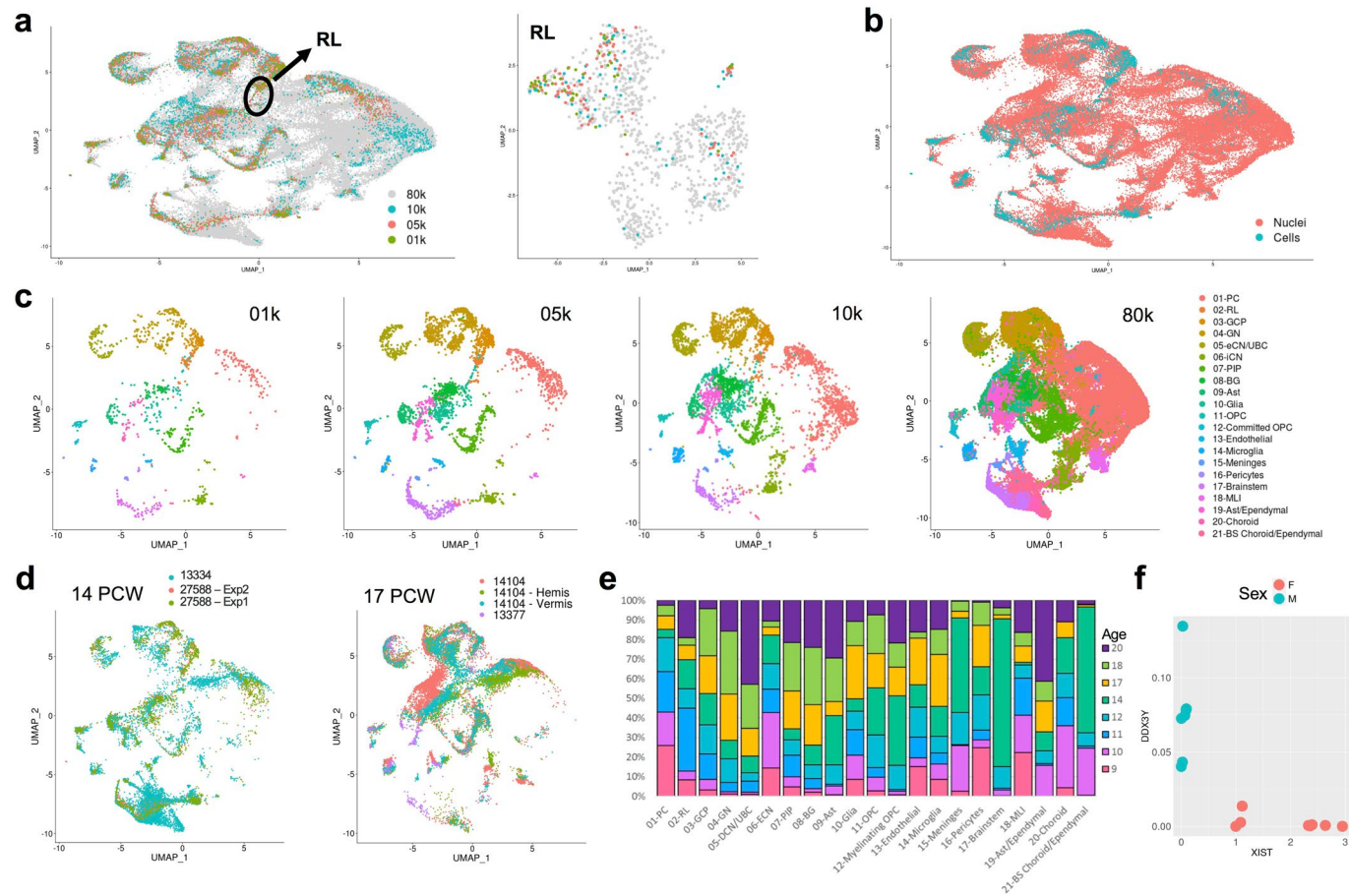
**Extended Data Fig. 2 | Co-expression modules in the developing human cerebellum.** Weighted gene co-expression network analysis (WGCNA) dendrogram identified 21 modules comprised of 6,336 expressed genes (row 1). M0 (grey) comprised of nonclustered genes was not analyzed further. Rows 2–4 show differential expression relationships between module genes and LCM-enriched region compared to bulk expression. EGL, external granule cell layer; PCL, Purkinje cell layer; RL, rhombic lip.



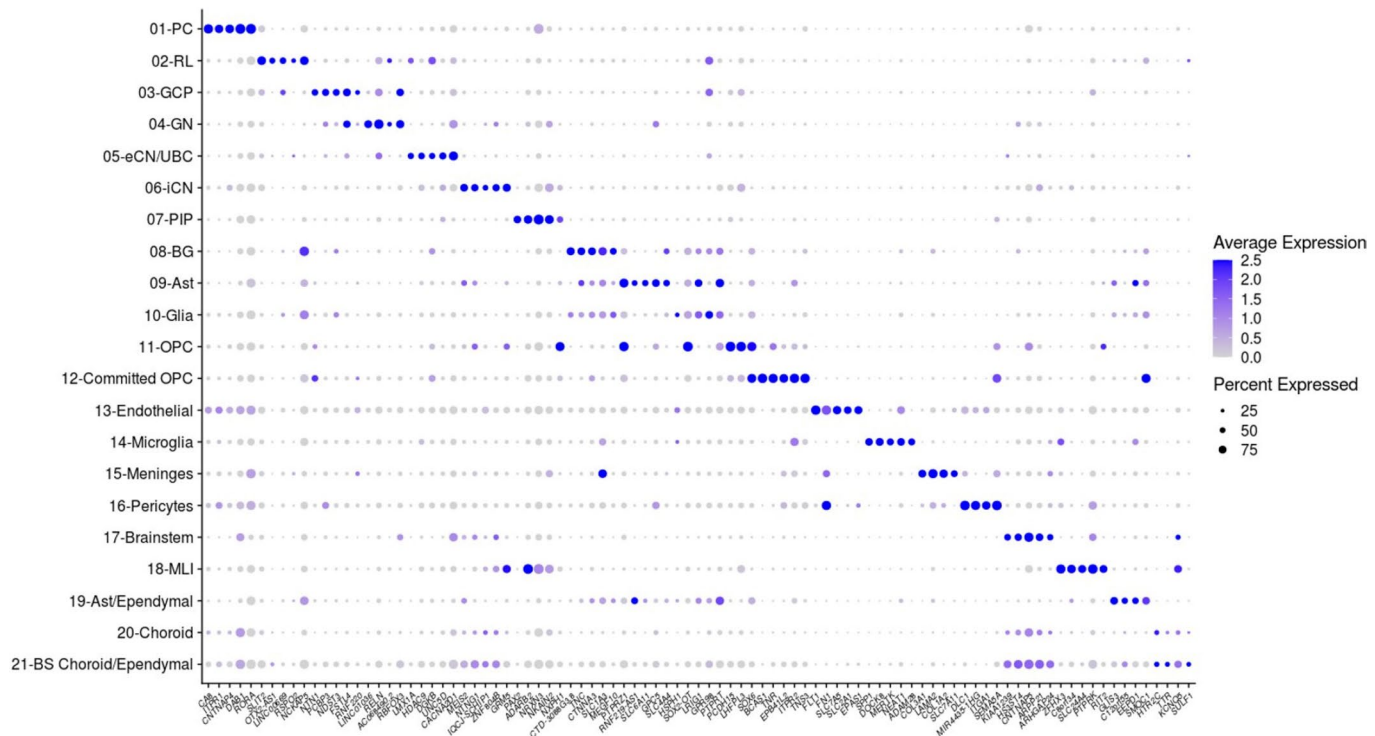
**Extended Data Fig. 3 | Co-expression modules in the developing human cerebellum by region.** Boxplots of gene expression per WGCNA module for bulk and spatial regions (box: 25–75<sup>th</sup> percentiles, whiskers: 10–90<sup>th</sup> percentiles, horizontal line in box: median). Number of genes per module: n=48 for M1; 81 for M2; 88 for M3; 40 for M4; 149 for M5; 79 for M6; 253 for M7; 283 for M8; 288 for M9; 102 for M10; 121 for M11; 87 for M12; 401 for M13; 136 for M14; 139 for M15; 317 for M16; 367 for M17; 182 for M18; 395 for M19; 327 for M20. EGL, external granule cell layer; PCL, Purkinje cell layer; RPKM, reads per kilobase of transcript per million mapped reads; RL, rhombic lip.



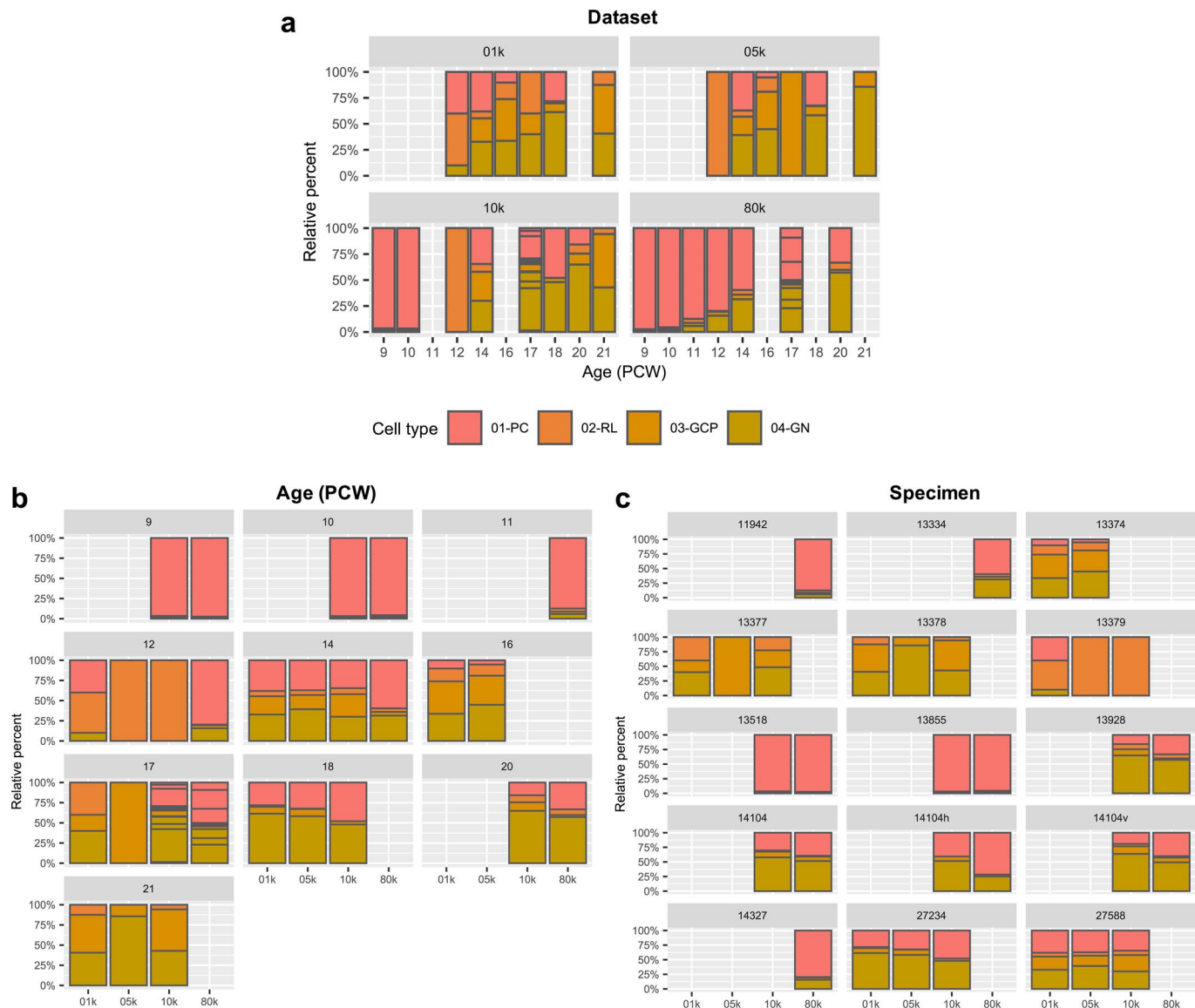
**Extended Data Fig. 4 | Co-expression modules in the developing human cerebellum by age.** LOESS expression values across development are shown with 95% CIs per module. Spatial regions are distinguished by colors: bulk (salmon); EGL (green); PCL (turquoise); RL (purple). EGL, external granule cell layer; PCW, postconceptional week; PCL, Purkinje cell layer; RPKM, reads per kilobase of transcript per million mapped reads; RL, rhombic lip.



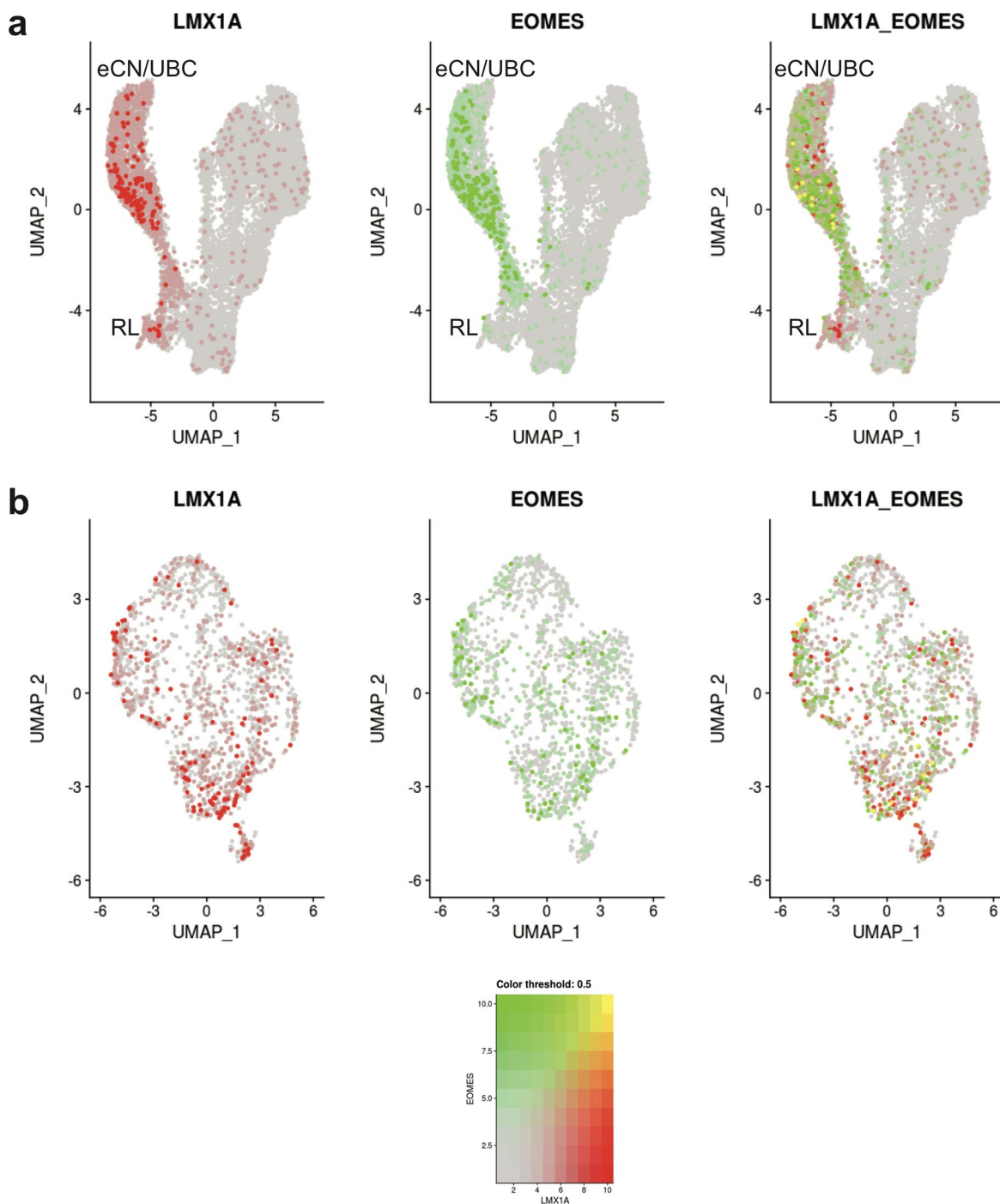
**Extended Data Fig. 5 | Quality control related analyses of snRNA-seq data.** **a**, UMAP visualization of 69,174 human cerebellar nuclei colored by dataset ( $n=1,076$  for 01k; 3,530 for 05k; 4,960 for 10k; 59,608 for 80k). Rhombic lip (RL) is circled. UMAP visualization of 1,018 RL nuclei colored by dataset at right (nuclei numbers:  $n=41$  for 01k; 88 for 05k; 67 for 10k; 822 for 80k). **b**, The same UMAP as in **a** with nuclei colored by type ( $n=4,462$  cells; 64,712 nuclei). **c**, The same UMAP as in **a** and **b** showing nuclei from each dataset. Nuclei are colored by cell type. **d**, The same UMAP as in **a-c** showing nuclei sampled from same age biological and technical replicates ( $n=11,213$  for 14 PCW; 8,453 nuclei for 13334; 2,098 cells for 27588 Exp1; 662 cells for 27588 Exp2;  $n=15,556$  for 17 PCW; 524 cells for 13377; 8,540 nuclei for 14104; 3,364 nuclei for 14104 h; 3,128 nuclei for 14104 v). **e**, Stacked bar chart shows the percentage of age sampled in each of the 21 cell types. Bar colors represent age sampled in postconceptional weeks (9-20 PCW). **f**, Expression of the female-specific non-coding RNA *XIST* and the chromosome Y specific gene *DDX3Y* show correct sex assignment for female (salmon) and male (turquoise) samples ( $n=14$  female; 12 male).



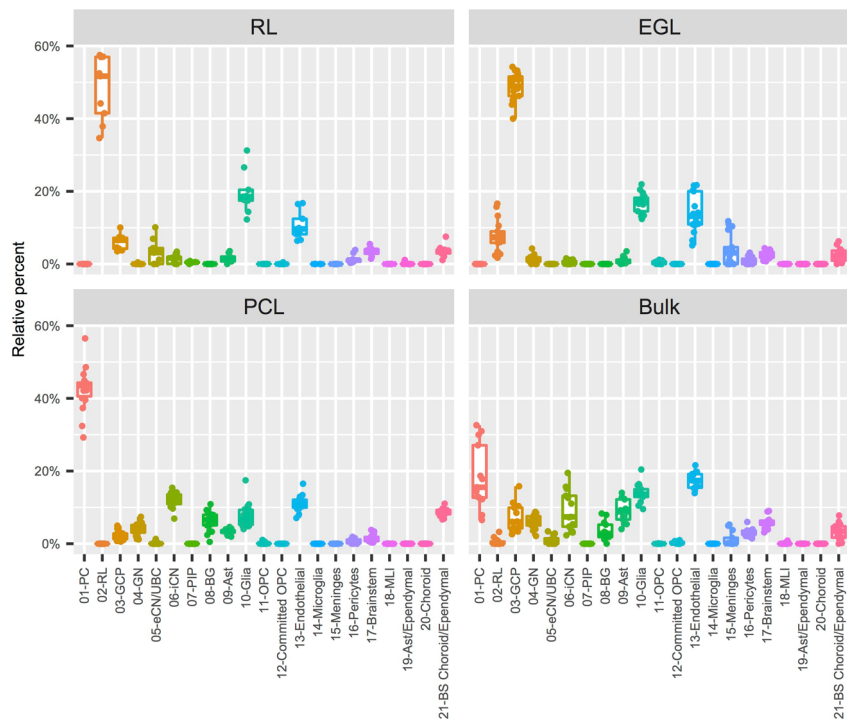
**Extended Data Fig. 6 | Cell-type-specific marker genes.** Dot plot showing expression of the top 5 most differentially expressed genes for each of the 21 cell types identified in early and mid-gestation fetal cerebellum. The size of the dot represents the percentage of cells within a cell type in which that gene was detected and its color represents the average expression level. Statistics are presented in Supplementary Table 9.



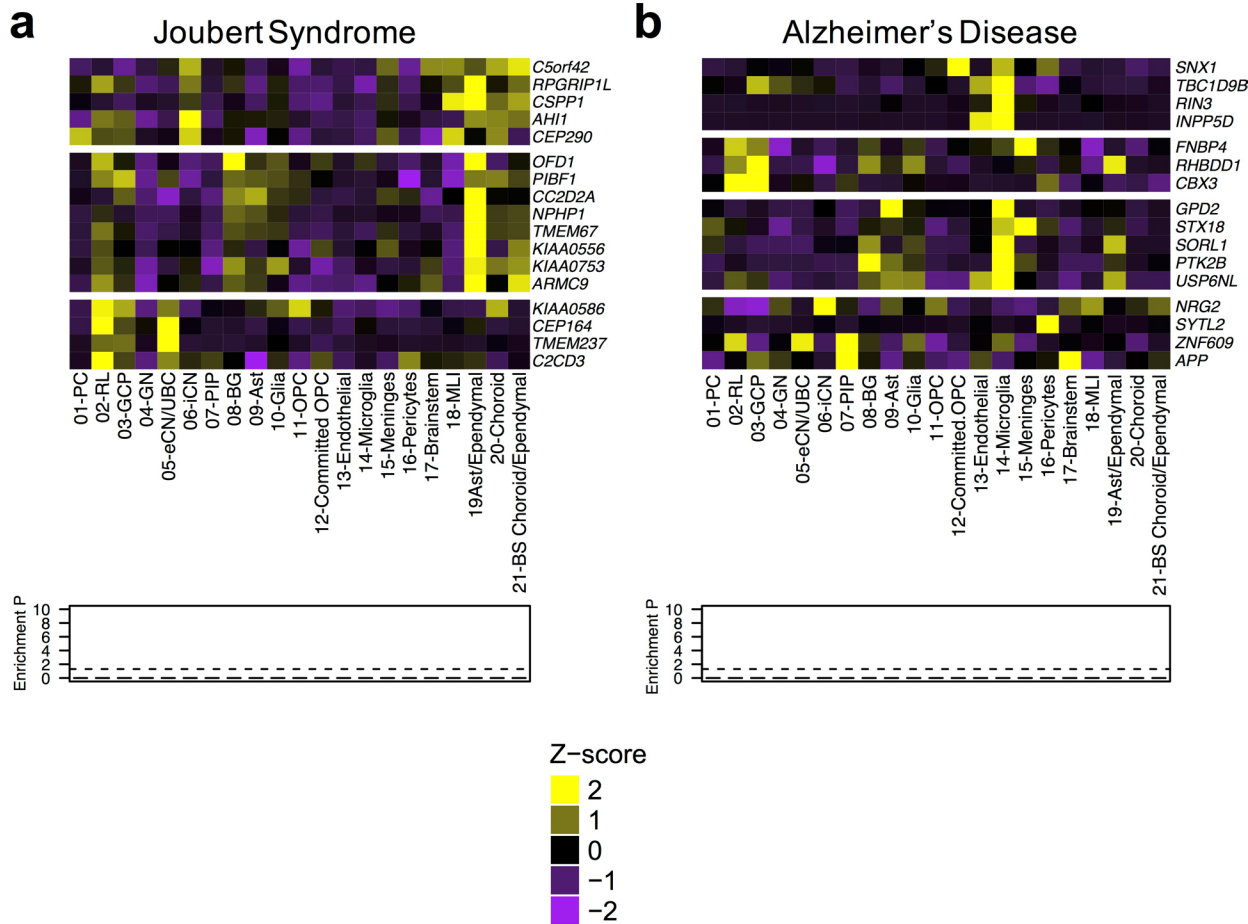
**Extended Data Fig. 7 | Distribution of major cell types.** **a-c**, Stacked bar charts show the percentage of the four major cell types from each dataset (a), developmental age (b), and specimen (c). Dataset 01k and 05k from experiment (Exp) 1 represent deep and shallow sequencing runs, respectively, from the same 6 samples (one per age). Dataset 10k from Exp 2 represents 11 samples (7 for a single age and 4 for 17 PCW), including 5 replicates from Exp 1. Dataset 80k from Exp 3 represents 9 samples (6 for a single age and 3 for 17 PCW), including 6 replicates from Exp 2. Sample and experiment characteristics are presented in Supplementary Tables 2 and 7.



**Extended Data Fig. 8 | Co-expression of marker genes in eCN/UBC.** **a**, The same UMAP visualization of cell types that originate from the RL as in Fig. 5a with nuclei colored by expression level for *LMX1A* (red), *EOMES* (green), and co-expression (yellow). **b**, The same UMAP visualization the eCN/UBC subcluster as in Fig. 5e with nuclei colored by expression level for *LMX1A* (red), *EOMES* (green), and co-expression (yellow).



**Extended Data Fig. 9 | Cell type heterogeneity in LCM-isolated regions of the cerebellum.** Box plots (box: 25–75<sup>th</sup> percentiles, whiskers: 10–90<sup>th</sup> percentiles, horizontal line in box: median) with data points (dots) showing the proportion of each of the 21 cell types from the *Developmental Cell Atlas of the Human Cerebellum* represented in the LCM RNA-seq data, grouped by LCM-isolated region. RL, rhombic lip; EGL, external granule cell layer; PCL, Purkinje cell layer.



**Extended Data Fig. 10 | Cerebellar cell type enrichment in Joubert syndrome and Alzheimer's disease.** Heatmaps of mean expression per fetal cerebellar cell type for genes associated with Joubert syndrome (**a**) or Alzheimer's disease (**b**). Color scheme is based on Z-score distribution. In the heatmaps, each row represents one gene and each column represents a single cell type. Horizontal white lines indicate branch divisions in the clustering dendograms (not shown). The full list of genes is provided in Supplementary Table 11. Enrichment P values (-Log10 P value) for each cell type are shown in the bottom bar plots. Significance determined by one-sample Z-test, two-tailed P value. The dashed line is the Bonferroni significance threshold ( $P < 0.05$ ); no gene enrichment was detected among the 21 cerebellar cell types.

## Reporting Summary

Nature Research wishes to improve the reproducibility of the work that we publish. This form provides structure for consistency and transparency in reporting. For further information on Nature Research policies, see our [Editorial Policies](#) and the [Editorial Policy Checklist](#).

### Statistics

For all statistical analyses, confirm that the following items are present in the figure legend, table legend, main text, or Methods section.

n/a Confirmed

- The exact sample size ( $n$ ) for each experimental group/condition, given as a discrete number and unit of measurement
- A statement on whether measurements were taken from distinct samples or whether the same sample was measured repeatedly
- The statistical test(s) used AND whether they are one- or two-sided  
*Only common tests should be described solely by name; describe more complex techniques in the Methods section.*
- A description of all covariates tested
- A description of any assumptions or corrections, such as tests of normality and adjustment for multiple comparisons
- A full description of the statistical parameters including central tendency (e.g. means) or other basic estimates (e.g. regression coefficient) AND variation (e.g. standard deviation) or associated estimates of uncertainty (e.g. confidence intervals)
- For null hypothesis testing, the test statistic (e.g.  $F$ ,  $t$ ,  $r$ ) with confidence intervals, effect sizes, degrees of freedom and  $P$  value noted  
*Give P values as exact values whenever suitable.*
- For Bayesian analysis, information on the choice of priors and Markov chain Monte Carlo settings
- For hierarchical and complex designs, identification of the appropriate level for tests and full reporting of outcomes
- Estimates of effect sizes (e.g. Cohen's  $d$ , Pearson's  $r$ ), indicating how they were calculated

*Our web collection on [statistics for biologists](#) contains articles on many of the points above.*

### Software and code

Policy information about [availability of computer code](#)

Data collection	RNAscope ISH and IHC images were acquired using the Zeiss Zen image software. SPLIT-seq .fastq into digital expression matrix: <a href="https://github.com/yjzhang/split-seq-pipeline">https://github.com/yjzhang/split-seq-pipeline</a>
Data analysis	LCM RNA-seq and SPLiT-seq data were analyzed in R studio 1.0.143 using R 3.3.3 STAR v2.5.3a Dobin et al., 2013 <a href="https://github.com/alexdobin/STAR">https://github.com/alexdobin/STAR</a> HTSeq Anders et al., 2015 <a href="https://htseq.readthedocs.io/en/master/index.html">https://htseq.readthedocs.io/en/master/index.html</a> DESeq2 v1.20.0 Love et al., 2014 <a href="https://bioconductor.org/packages/release/bioc/html/DESeq2.html">https://bioconductor.org/packages/release/bioc/html/DESeq2.html</a> RNA-SeQC v1.1.8 DeLuca et al., 2012 <a href="https://github.com/getzlab/rnaseqc">https://github.com/getzlab/rnaseqc</a> WGCNA Zhang & Horvath 2005 <a href="https://cran.r-project.org/web/packages/WGCNA/index.html">https://cran.r-project.org/web/packages/WGCNA/index.html</a> Seurat v3.0 Butler et al., 2018 <a href="https://satijalab.org/seurat/">https://satijalab.org/seurat/</a> Monocle 3 Cao et al., 2019 <a href="http://cole-trapnell-lab.github.io/monocle-release/">http://cole-trapnell-lab.github.io/monocle-release/</a> CIBERSORTx Newman et al., 2019 <a href="https://cibersortx.stanford.edu/">https://cibersortx.stanford.edu/</a> LIGER Welsh et al., 2019 <a href="https://github.com/welch-lab/liger">https://github.com/welch-lab/liger</a>

For manuscripts utilizing custom algorithms or software that are central to the research but not yet described in published literature, software must be made available to editors and reviewers. We strongly encourage code deposition in a community repository (e.g. GitHub). See the Nature Research [guidelines for submitting code & software](#) for further information.

## Data

Policy information about [availability of data](#)

All manuscripts must include a [data availability statement](#). This statement should provide the following information, where applicable:

- Accession codes, unique identifiers, or web links for publicly available datasets
- A list of figures that have associated raw data
- A description of any restrictions on data availability

Processed data are available through the Human Cell Atlas (<https://www.covid19cellatlas.org/aldinger20>), the UCSC Cell Browser (<https://cbl-dev.cells.ucsc.edu>), and upon request. Sequence data were deposited into the Database of Genotypes and Phenotypes (dbGaP), under accession number and phs001908.v2.p1, and available upon request.

Other data used include the BrainSpan RNA-seq dataset (<http://www.brainspan.org/static/download.html>).

## Field-specific reporting

Please select the one below that is the best fit for your research. If you are not sure, read the appropriate sections before making your selection.

Life sciences       Behavioural & social sciences       Ecological, evolutionary & environmental sciences

For a reference copy of the document with all sections, see [nature.com/documents/nr-reporting-summary-flat.pdf](https://nature.com/documents/nr-reporting-summary-flat.pdf)

## Life sciences study design

All studies must disclose on these points even when the disclosure is negative.

Sample size	Sample sizes for each experiment are detailed in the manuscript. No statistical methods were used to predetermine sample sizes. Sample sizes were chosen based on the ability to obtain representative data across a range of ages.
Data exclusions	Data were filtered according to analysis criteria described in the manuscript. In RNA-sequencing analyses, we excluded 6 samples because principal component analysis separated these samples from all others. In single-nucleus analyses, we excluded nuclei with <200 genes, >4 standard deviations above the median number of genes or unique molecular identifiers, or >1-5% mitochondrial genes.
Replication	Results highlighted in the manuscript were reproduced using independent methodologies (LCM RNA-seq, SPLiT-seq, RNAscope ISH, and IHC).
Randomization	No randomization was used since there was no treatment in this study.
Blinding	Blinding was not performed because knowledge of experimental conditions was required during data collection and analyses. All samples were treated equally using the same rigorous criteria to avoid bias.

## Reporting for specific materials, systems and methods

We require information from authors about some types of materials, experimental systems and methods used in many studies. Here, indicate whether each material, system or method listed is relevant to your study. If you are not sure if a list item applies to your research, read the appropriate section before selecting a response.

### Materials & experimental systems

n/a	Involved in the study
<input type="checkbox"/>	Antibodies
<input checked="" type="checkbox"/>	Eukaryotic cell lines
<input checked="" type="checkbox"/>	Palaeontology and archaeology
<input checked="" type="checkbox"/>	Animals and other organisms
<input type="checkbox"/>	Human research participants
<input checked="" type="checkbox"/>	Clinical data
<input checked="" type="checkbox"/>	Dual use research of concern

### Methods

n/a	Involved in the study
<input checked="" type="checkbox"/>	ChIP-seq
<input checked="" type="checkbox"/>	Flow cytometry
<input checked="" type="checkbox"/>	MRI-based neuroimaging

## Antibodies

### Antibodies used

Calbindin (Swant, CB38, rabbit, 1:3000), PAX6 (Biolegend, 901301, rabbit, 1:300), SKOR2 (Novus, NBP2-14565, rabbit, 1:100), and NEUN (Millipore, MAB377, mouse, 1:100).

### Validation

Well characterized commercial antibodies were used.

CB38 Swant: raised against recombinant rat calbindin D-28k. Western Blot analysis shows validation at 28 kDa.

Immunohistochemistry in the cerebellum of Calbindin D-28k knock-out mouse shows an absence of staining. [https://www.swant.com/pdfs/CB38\\_Rabbit anti Calbindin D-28k 500 ul.pdf](https://www.swant.com/pdfs/CB38_Rabbit%20anti%20Calbindin%20D-28k%20500%20ul.pdf)

PAX6 Biolegend, 901301: generated against the peptide (QVPGSEPDMSQYWPRLQ) derived from the C-terminus of the mouse Pax6 protein. Each lot of this antibody is quality control tested by Western blotting and formalin-fixed paraffin-embedded immunohistochemical staining of brain tissue.

SKOR2 Novus, NBP2-14565: raised against recombinant protein corresponding to amino acids: MASSPLPGPNNDILLASPSSAFQPDTLSQPRPGHANLKPQVGQVILYGIPIVS. Verified on a Protein Array containing target protein plus 383 other non-specific proteins. <https://www.novusbio.com/PDFs/NBP2-14565.pdf>

NEUN Millipore, MAB377: Cone A60 detects level of NeuN and has been published and validated for use in FC, IC, IF, IH, IH(P), IP and WB. [https://www.emdmillipore.com/US/en/product/Anti-NeuN-Antibody-clone-A60,MM\\_NF-MAB377#overview](https://www.emdmillipore.com/US/en/product/Anti-NeuN-Antibody-clone-A60,MM_NF-MAB377#overview)

## Human research participants

Policy information about [studies involving human research participants](#)

Population characteristics

Specimens were obtained from the Birth Defects Research Laboratory or the Human Developmental Biology Resource tissue repositories. A total of 29 histologically normal cerebella were collected. Due to the sensitivity of the samples, population characteristics were not recorded.

Recruitment

No recruitment criteria other than consent was required.

Ethics oversight

This study was performed in accordance with ethical and legal guidelines of the Seattle Children's Hospital institutional review board. Informed consent was obtained prior to sample collection and for use in this study.

Note that full information on the approval of the study protocol must also be provided in the manuscript.